A Mid-infrared Flare in the Active Galaxy MCG-02-04-026: Dust Echo of a Nuclear Transient Event

Luming Sun[1,2] , Ning Jiang[1,2] , Tinggui Wang[1,2] , Hongyan Zhou[1,2,3] , Liming Dou[4] , Chenwei Yang[3], Xiang Pan[3] ,
Zhenfeng Sheng[1,2] , Zhihao Zhong[1,2], Lin Yan[5] , and Ge Li[1]

[1] Key Laboratory for Research in Galaxies and Cosmology, Department of Astronomy, University of Science and Technology of China, Chinese Academy of Sciences, Hefei, Anhui 230026, People's Republic of China; lmsun@ustc.edu.cn, jnac@ustc.edu.cn
[2] School of Astronomy and Space Science, University of Science and Technology of China, Hefei 230026, People's Republic of China
[3] Polar Research Institute of China, 451 Jinqiao Road, Shanghai, People's Republic of China
[4] Center for Astrophysics, Guangzhou University, Guangzhou, 510006, People's Republic of China
[5] Caltech Optical Observatories, Cahill Center for Astronomy and Astrophysics, California Institute of Technology, Pasadena, CA 91125, USA

Abstract

We report the discovery of a mid-infrared (MIR) flare using Wide field Infrared Survey Explorer data in the center of the nearby Seyfert 1.9 galaxy MCG-02-04-026. The MIR flare began in the first half of 2014, peaked around the end of 2015, and faded in 2017. During these years, energy of more than 7×10^{50} erg was released in the infrared, and the flare's MIR color was generally turning red. We detected neither optical nor ultraviolet (UV) variation corresponding to the MIR flare based on available data. We explained the MIR flare using a dust echo model in which the radiative transfer is involved. The MIR flare can be well explained as thermal reradiation from dust heated by UV–optical photons of a primary nuclear transient event. Although the transient event was not seen directly owing to dust obscuration, we can infer that it may produce a total energy of at least $\sim 10^{51}$ erg, most of which was released in less than $\sim$3 yr. The nature of the transient event could be a stellar tidal disruption event by the central supermassive black hole (SMBH), or a sudden enhancement of the existing accretion flow onto the SMBH, or a supernova that was particularly bright.

Unified Astronomy Thesaurus concepts: Transient sources (1851); Infrared astronomy (786); Active galaxies (17)

1. Introduction

Recently, in the nuclear regions of some active galaxies, transient events involving rapid and great rise in the luminosity have been reported. The examples are CSS100217:102913 +404220 (Drake et al. 2011), PS16dtm (Blanchard et al. 2017), an event in F01004-2237 (Tadhunter et al. 2017), PS1-10adi (Kankare et al. 2017), an event in W0948+0318 (Kankare et al. 2017; Assef et al. 2018), AT 2017bgt (Trakhtenbrot et al. 2019), OGLE17aaj (Gromadzki et al. 2019), and some more (see Lawrence et al. 2016; Graham et al. 2017; Kankare et al. 2017; Kostrzewa-Rutkowska et al. 2018; Drake et al. 2019; etc.). During these events, the galactic nuclei reached their peak luminosities in 1–2 months with their magnitudes decreasing by ∼1 mag or even more, out of the common range of active galactic nucleus (AGN) variabilities (generally less than 0.5 mag; Caplar et al. 2017). The nuclei then gradually faded, and their luminosities returned to the initial levels in a half to a couple of years. These events evolved much faster than another type of AGN transient event with timescales of 10 yr or longer, such as Mrk 1018 (McElroy et al. 2016) and Mrk 590 (Denney et al. 2014), which were called "changing-look AGNs" owing to the changes in their spectral types.

The natures of these transient events are not entirely understood. Researchers have suggested three possible origins for these events, including stellar tidal disruption events (TDEs) by the central supermassive black hole (SMBH; e.g., Blanchard et al. 2017; Tadhunter et al. 2017), superluminous supernovae (SLSNe) (e.g., Drake et al. 2011), and an enhancement of the existing accretion flow of the AGN (e.g., Gromadzki et al. 2019; Trakhtenbrot et al. 2019). TDEs and SLSNe are rare and bright transient events that were first recognized in inactive galaxies. A TDE occurs when a star

passes by an SMBH and is tidally disrupted (e.g., Rees 1988). The disrupted stellar materials are then accreted by the SMBH, generating a luminous flare. The flare's luminosity peaks in months or shorter and then decreases over a period of months to years (Komossa 2015). The TDE flare can cause the inactive galaxy that it resides in to temporarily look like an active galaxy. SLSNe (e.g., Gal-Yam 2012) are a rare class of supernovae (SNe) that are particularly bright (less than −21 in magnitude in optical; Moriya et al. 2018). Their luminosities, duration time, and the shapes of their light curves (LC) are similar to those of TDEs. The nature of SLSNe and the reason why they are so bright are still unclear. According to their spectra, SLSNe can be divided into two types. One type is SLSNe-I with no hydrogen lines, and the other type is SLSNe-II with hydrogen lines, and the spectral behaviors of some SLSNe-II can be similar to those of TDEs and AGNs. The timescale, energy budget, and spectral features of most of the transient events in active galaxies mentioned in the first paragraph are similar to those of TDEs and SLSNe-II in inactive galaxies; thus, they may be these two types of events that occur in active galaxies. Sometimes, the LC or spectral features of some transient events are difficult to explain with TDEs or SLSNe-II, and researchers tended to interpret them as sudden enhancements of the existing accretion flow onto the SMBH (e.g., Trakhtenbrot et al. 2019), though the reason why the accretion rate can change drastically in such a short time is not clear (see Lawrence 2018). Because the phenomena produced by these three possible origins are similar, despite great efforts of researchers, no unambiguous conclusions can be reached on the nature of the transient events in active galaxies.

Many of the transient events in active galaxies are accompanied by mid-infrared (MIR) flares. The examples are CSS100217:102913+404220 (Jiang et al. 2019), PS16dtm (Jiang et al. 2017), F01004-2237 (Dou et al. 2017), PS1-10adi (Kankare et al. 2017), W0948+0318 (Assef et al. 2018), and OGLE17aaj (Yang et al. 2019). The MIR flares were observed by an all-sky time-domain survey in the MIR band named the Wide field Infrared Survey Explorer (WISE), which we will introduce in detail later. The MIR flares generally lasted for several to 10 yr, during which they dramatically strengthened the MIR radiation of the galaxies as the magnitudes of the galaxies decreased by a half to several magnitudes.

On the origin of the accompanied MIR flares in the transient events, a promising interpretation is that the MIR flares come from dust echoes of the transient events. The dust echo has been modeled by Lu et al. (2016) and Jiang et al. (2017). Briefly, when a transient event occurs in a galactic nucleus, its growing UV–optical radiation sublimates the dust in the environment continuously, forcing the dust to form inner surfaces with increasing radii. When the UV–optical radiation declines, it can no longer sublimate the dust, and hence the radius of the inner surface stops increasing. The UV–optical radiation heats the dust around the eventual inner surface, and meanwhile it is converted to IR reradiation by the dust. The model is supported by increasing observational evidence. The MIR radiation peaked later than the UV–optical radiation, and there is a rough relationship between the time delay τ between UV–optical and MIR radiations and the sublimation radius (r_{sub}) corresponding to the peak luminosity (L_{max}) of the transient event: $\tau \sim R_{sub}(L_{max})/c$ (e.g., Dou et al. 2017; Jiang et al. 2017). The relationship is the observational evidence that the echoing dust is located around the eventual inner surface. Blanchard et al. (2017) found that PS16dtm, a transient event hosted in a narrow-line Seyfert 1 galaxy with existing Fe II emission, enhanced the Fe II emission in half a year after the transient event's flux peaks. Also, Jiang et al. (2019) noticed that along with PS1-10adi, transient Fe II emission increased rapidly around the time of the optical maximum and disappeared in an observation 3.5 yr later. These transient Fe II emissions that varied on a timescale of years were interpreted as the radiation of Fe elements in the dust clouds that is released from the solid state into the gas state under UV photons (Jiang et al. 2019). They are the observational evidence of the dust sublimation in the model.

The dust in the nuclear region not only can produce an MIR flare by echo but also can obscure the UV and optical radiation of a transient event if the dust is located on the line of sight. Hence, if the dust obscuration is severe, the dust can hide the transient event from us in optical surveys. Hidden transient events in active galaxies may be common, considering that more than half of active galaxies belong to type II or type 1.9, as their nuclei are severely obscured by dust. The hidden transient events disturb the statistics of the transient events. For an accurate statistics, methods other than optical surveys are required to detect the hidden transient events. MIR radiation is little affected by dust extinction, and thus the hidden transient events in active galaxies can be found using accompanied MIR flares as probes. An example is an IR flare named Arp 299-B AT1 (Mattila et al. 2018), which was discovered with ground-based near-infrared (NIR) observations and Spitzer MIR observations. It occurred at the nucleus of Arp 299-B1, which hosts a Compton-thick AGN. It caused the IR luminosity of the nucleus to rise continuously and reach the peak during ∼5 yr and then decrease at a lower rate. It released a total IR energy of $>10^{52}$ erg over a duration of more than 10 yr. The IR flare was accompanied by a weak optical variation discovered by the Hubble Space Telescope (HST) that could be related to it. The optical variation was so weak that it might have been missed if the IR flare had not been discovered first or the galaxy had not been observed by HST many times. The IR flare was also accompanied by a transient radio jet, based on which Mattila et al. demonstrated that the IR flare was caused by a TDE. Recently, Kool et al. (2020) discovered a similar IR transient AT 2017gbl through Kbandobservations in luminous IR galaxy IRAS 23436+5257, which also hosts an obscured AGN. The transient was accompanied by a radio transient, and in its optical and NIR spectra the fluxes of broad emission lines decreased with time. Based on these facts, Kool et al. interpreted the transient as an obscured accretion event by the central supermassive black hole

The WISE (Wright et al. 2010) survey is a powerful tool for finding the hidden transient events via accompanied MIR flares. The WISE telescope has been conducting a repetitive all-sky survey since 2010. The survey was named WISE, NEOWISE (Mainzer et al. 2011), and NEOWISE-R (Mainzer et al. 2014) at different times. Every half a year, except for a hiatus between 2011 and 2013, WISE took multiple exposures during several days for a certain sky region. The observations were initially carried out with four MIR filters with central wavelengths of 3.4, 4.6, 12, and 22 μm, named $W1$ to $W4$, and then with only the $W1$ and $W2$ filters after the cryogen was exhausted in 2010 September. For all galaxies, WISE observations provide information of variabilities on timescales of hours, days, and years. There have been works that search for MIR flares with variability timescales of years using WISE data. Wang et al. (2018) found 14 normal galaxies with long-term declining MIR radiations and argued that the MIR variations may be caused by TDEs. Assef et al. (2018) found nine galaxies whose MIR LCs resemble that of W0948+0318, none of which showed an optically detected transient event. Yang et al. (2019) reported an MIR flare in a type II AGN, J1657+2345, with no significant changes in the optical.

We are conducting a comprehensive search of MIR flares in nearby Sloan Digital Sky Survey (SDSS) spectroscopic galaxies using WISE data (Jiang et al. 2020). We found several tens of MIR flares. Some of them are in active galaxies, and a large fraction of them have no accompanied optical transient events detected. We aim to extract as much information as possible about the transient events that caused the MIR flares based on only MIR data. The information will help us understand the nature of the MIR flares. We made an attempt using an MIR flare in MCG-02-04-026, which is a $z = 0.03485$ edge-on disk galaxy located at $\alpha_{J2000} = 01{:}20{:}47.99$, $\delta_{J2000} = -08{:}29{:}18.4$. In this paper, we will present observations and data of the galaxy in Section 2, analyze the data in Section 3, model the MIR data and extract information about the primary transient event in Section 4, and finally explore the nature of the MIR flare in Section 5. Throughout this paper, we use cosmological parameters of $H_0 = 67 \, \mathrm{km \, s^{-1} \, Mpc^{-1}}$, $\Omega_m = 0.32$, and $\Omega_\Gamma = 0.68$, resulting in a luminosity distance of 160 Mpc for MCG-02-04-026.

Table 1
A Summary of the Observations of MCG-02-04-026

Year	Radio	FIR	MIR	NIR		Optical		UV	X-Ray
	⋯	phot	phot	phot	spec	phot	spec	phot	⋯
1983		IRAS							
1991									ROSAT
1997	VLA								
1998				2MASS					
2003								GALEX	
2005–2008						CSS			
2009						(2005–2013)		SDSS	
2010			WISE			SDSS			
2011–2012						(2009)			
2013						PTF	BOSS		
2014						(2009–2012)			
2015			Neo-			ASAS-SN		SWIFT/UVOT	SWIFT/XRT
2016–2017			WISE			(2012–2018)			
2018				TPSP			DBSP	SWIFT/UVOT	SWIFT/XRT

Note. "phot" stands for photometric observations, and "spec" stands for spectroscopic observations.

Table 2
Logs of WISE Observations of MCG-02-04-026 and Binned PSF Magnitudes

Date	MJD	N_{image}[a]	N_{good}[a]	Co-add[b]	Magnitude			
					$W1$	$W2$	$W3$	$W4$
2010 Jul 8	55386	13	12	yes	11.02 ± 0.05	10.48 ± 0.04	7.32 ± 0.03	5.38 ± 0.07
2010 Dec 31	55562	10	9	yes	10.99 ± 0.05	10.45 ± 0.04		
2014 Jan 2	56660	12	8	yes	10.99 ± 0.02	10.47 ± 0.01		
2014 Jul 9	56848	12	10	yes	10.71 ± 0.02	10.18 ± 0.03		
2015 Jan 4	57027	11	8	yes	10.68 ± 0.02	10.03 ± 0.03		
2015 Jul 6	57210	25	11	yes	10.62 ± 0.02	9.94 ± 0.02		
2015 Dec 29	57386	13	10	yes	10.58 ± 0.05	9.90 ± 0.04		
2016 Jul 7	57577	11	10	yes	10.65 ± 0.03	9.92 ± 0.02		
2016 Dec 22	57745	12	8	yes	10.89 ± 0.05	10.10 ± 0.03		
2017 Jul 6	57941	13	8	yes	10.97 ± 0.03	10.35 ± 0.01		
2017 Dec 18	58106	14	8	no	11.09 ± 0.03	10.54 ± 0.04		
2018 Jul 8	58308	22	10	no	10.90 ± 0.04	10.29 ± 0.05		

Notes.
[a] Number of images taken during this observation, and number of good photometric data.
[b] Whether a co-added image from this observation is available from Meisner et al. (2018) or not.

2. Observations and Data

In Table 1 we list the basic information of all the observations of which the data were used in this paper. The information includes the time, the band, the instrument, and the mode (photometric/spectroscopic). We described the details of the observations and the data in the following.

2.1. WISE Photometric Data

As we have mentioned, WISE took multiple exposures of each target within several days every half a year. We referred to the multiple exposures as an observation. For MCG-02-04-026, data from 12 observations had been published. We list the information of the 12 observations in Table 2. The first two observations are in 2010, and the remaining are during 2013 and 2018. The first observation took images with all four filters, and the remaining observations only took images with $W1$ and $W2$ filters. In each band of each observation, there were 10–25 exposures and images of the same number were obtained.

The WISE pipeline has performed photometries of each target by fitting the images with point-spread functions (PSFs). We collected the PSF magnitudes of MCG-02-04-026 from the NASA/IPAC InfRared Science Archive (IRSA).[6] We removed the bad magnitudes with poor image quality (qi_fact = 0), charged particle hits (saa_sep < 0), scattered moonlight (moon_masked = 1), or artifacts (cc_flags > 0), and there were 8-12 good magnitudes left in each band of each observation. We did not detect any variations in any band of any observation. So we binned the magnitudes in each band of each observation by taking the mean value and the standard deviation of the magnitudes as the value and the error, respectively. The binned magnitudes were listed in Table 2.

Meisner et al. (2018) provided time-resolved WISE/NEOWISE co-added images of each observation. For MCG-02-04-026, the co-added images from the first 10 observations had been published.[7]

Table 3
Logs of Optical Photometry of MCG-02-04-026 and Binned LC

Time (MJD)	Magnitude	Time (MJD)	Magnitude	Time (MJD)	Magnitude	Time (MJD)	Magnitude
CSS		2010-01(55216)	14.85 ± 0.04	2012-11(56244)	15.22 ± 0.02	2016-05(57531)	15.33 ± 0.06
2005-08(53595)	14.75 ± 0.04	2010-10(55489)	14.72 ± 0.02	2012-12(56272)	15.24 ± 0.04	2016-06(57554)	15.18 ± 0.03
2005-09(53627)	14.74 ± 0.02	2010-11(55508)	14.72 ± 0.03	2013-01(56317)	15.18 ± 0.06	2016-07(57588)	15.29 ± 0.04
2005-10(53655)	14.74 ± 0.02	2010-12(55536)	14.72 ± 0.03	2013-06(56465)	15.19 ± 0.03	2016-08(57614)	15.23 ± 0.04
2005-11(53691)	14.74 ± 0.02	2011-01(55575)	14.73 ± 0.03	2013-07(56488)	15.20 ± 0.02	2016-09(57648)	15.32 ± 0.04
2005-12(53721)	14.73 ± 0.02	2011-07(55774)	14.82 ± 0.04	2013-08(56520)	15.21 ± 0.04	2016-10(57677)	15.25 ± 0.02
2006-08(53952)	14.82 ± 0.04	2011-09(55827)	14.77 ± 0.03	2013-09(56553)	15.30 ± 0.06	2016-11(57709)	15.27 ± 0.02
2006-09(54003)	14.72 ± 0.03	2011-10(55857)	14.73 ± 0.02	2013-10(56571)	15.22 ± 0.02	2016-12(57742)	15.30 ± 0.03
2006-10(54025)	14.73 ± 0.02	2011-11(55887)	14.75 ± 0.02	2013-12(56641)	15.25 ± 0.02	2017-01(57766)	15.30 ± 0.03
2006-11(54059)	14.73 ± 0.02	2011-12(55923)	14.74 ± 0.03	2014-01(56676)	15.28 ± 0.05	2017-05(57901)	15.11 ± 0.06
2006-12(54088)	14.71 ± 0.02	2012-10(56215)	14.74 ± 0.02	2014-06(56831)	15.28 ± 0.05	2017-06(57922)	15.26 ± 0.06
2007-06(54266)	14.84 ± 0.04	2012-11(56233)	14.76 ± 0.03	2014-07(56852)	15.29 ± 0.05	2017-07(57952)	15.27 ± 0.03
2007-08(54333)	14.82 ± 0.04	2013-01(56305)	14.69 ± 0.03	2014-08(56888)	15.28 ± 0.02	2017-08(57980)	15.31 ± 0.03
2007-09(54352)	14.72 ± 0.02	2013-07(56478)	14.81 ± 0.03	2014-09(56916)	15.29 ± 0.04	2017-09(58014)	15.28 ± 0.03
2007-10(54386)	14.72 ± 0.02	2013-09(56557)	14.74 ± 0.02	2014-10(56946)	15.29 ± 0.02	2017-10(58047)	15.23 ± 0.03
2007-11(54408)	14.70 ± 0.03	2013-10(56585)	14.73 ± 0.02	2014-11(56977)	15.24 ± 0.02	2017-11(58071)	15.26 ± 0.04
2008-01(54468)	14.72 ± 0.03	PTF		2014-12(57006)	15.27 ± 0.04	2017-12(58099)	15.23 ± 0.05
2008-08(54684)	14.81 ± 0.04	2009-07(55044)	14.75 ± 0.04	2015-01(57035)	15.25 ± 0.02	2018-01(58130)	15.31 ± 0.04
2008-09(54722)	14.73 ± 0.02	2009-08(55061)	14.74 ± 0.02	2015-05(57164)	15.31 ± 0.04	2018-06(58288)	15.32 ± 0.03
2008-10(54765)	14.77 ± 0.03	2009-09(55088)	14.74 ± 0.02	2015-06(57188)	15.26 ± 0.04	2018-07(58319)	15.35 ± 0.02
2008-11(54787)	14.74 ± 0.02	2009-11(55152)	14.74 ± 0.02	2015-07(57222)	15.26 ± 0.04	2018-08(58349)	15.31 ± 0.02
2009-01(54833)	14.82 ± 0.04	2010-09(55460)	14.73 ± 0.02	2015-08(57253)	15.30 ± 0.04	2018-09(58371)	15.28 ± 0.01
2009-08(55060)	14.69 ± 0.03	2011-12(55903)	14.82 ± 0.04	2015-09(57280)	15.26 ± 0.04	2018-10(58413)	15.31 ± 0.03
2009-09(55099)	14.72 ± 0.03	2012-10(56228)	14.72 ± 0.03	2015-10(57313)	15.23 ± 0.03	2018-11(58443)	15.40 ± 0.03
2009-10(55127)	14.73 ± 0.02	2012-11(56235)	14.73 ± 0.02	2015-11(57339)	15.28 ± 0.03		
2009-11(55148)	14.73 ± 0.02	ASAS-SN		2015-12(57372)	15.27 ± 0.03		
2009-12(55182)	14.74 ± 0.03	2012-10(56220)	15.24 ± 0.02	2016-01(57401)	15.23 ± 0.04		

2.2. Time-domain Photometric/Imaging Data and X-Ray Data

We collected optical photometric data of MCG-02-04-026 from three transient surveys, Catalina Sky Survey (CSS; Drake et al. 2009), Palomar Transient Factory (PTF; Law et al. 2009), and All-Sky Automated Survey for Supernovae (ASAS-SN; Shappee et al. 2014; Kochanek et al. 2017).[8] MCG-02-04-026 was observed by CSS with the V_{CSS} filter over 42 months (66 nights) from 2005 August to 2013 October, by PTF with the R filter over 8 months (17 nights) from 2009 July to 2012 November, and by ASAS-SN with the V filter over 52 months (409 nights) from 2012 October to 2018 November. For each survey, we binned the photometric data taken in each month to obtain an LC using the same method as we did for the WISE/NEOWISE data. The binned LCs are listed in Table 3.

We collected UV imaging data and X-ray data of MCG-02-04-026. We found archival UV imaging data from SDSS observations with the SDSS u filter in 2009 October, GALEX observations with the far-UV (FUV) and near-UV (NUV) filters in 2013 October, and SWIFT/UVOT observations with the UVW2 filter in 2015 May. We also found archival X-ray data from ROSAT/PSPC All-Sky Survey (RASS) observations taken between 1990 July and 1991 January and SWIFT/XRT observations taken in 2015 May. We applied for a new SWIFT target-of-opportunity observation of MCG-02-04-026, and the observation was taken in 2018 June. An image was obtained by SWIFT/UVOT with the U filter, and X-ray data were obtained by SWIFT/XRT. We listed the basic information of the UV and X-ray observations in Table 4.[9]

2.3. Optical and NIR Spectral Data

We collected an archival optical spectrum of MCG-02-04-026 from SDSS-III's Baryon Oscillation Spectroscopic Survey (BOSS).[10] The spectrum was taken on 2013 November with a total exposure time of 7200 s, a wavelength coverage of 3600–10400 Å, and a spectral resolution of 1500–2500.

We took follow-up quasi-instantaneous optical and NIR spectroscopic observations of MCG-02-04-026 in 2018 January. The optical spectrum was taken on 2018 January 5 with the Double Spectrograph (DBSP) on the Hale 200-inch telescope at Palomar Observatory, and the NIR spectrum was taken on 2018 January 3 with the TripleSpec (TPSP) spectrograph on the same telescope. For the DBSP observation, we used a D55 dichroic, a 600/4000 grating for the blue side, and a 316/7500 grating for the red side. We adjusted the grating angles to obtain a nearly continuous wavelength coverage from 3200 to 10000 Å except for a small gap of 5470–5490 Å. We used a slit with 1″0 width because the seeing FWHM was ∼1″2, and we oriented the slit in the north–south direction, which is close to the direction of the galaxy disk. We took two exposures in order to remove cosmic rays. The total exposure time was 20 minutes. We took Fe–Ar and He–Ne–Ar

---

[8] We collected CSS photometries from CSS data release 2 (http://nesssi.cacr.caltech.edu/DataRelease/), PTF photometries from IRSA, and ASAS-SN photometries from their database (https://asas-sn.osu.edu/).

[9] We collected the SDSS image from SDSS DR12 (https://www.sdss.org/dr12/), the GALEX image from GALEX DR6 (http://galex.stsci.edu/GR6/), and SWIFT/UVOT images, SWIFT/XRT event files, and ROSAT/PSPC event files from the High Energy Astrophysics Science Archive Research Center (HEASARC) (https://heasarc.gsfc.nasa.gov/).

[10] We downloaded the spectrum from SDSS DR12.

Table 4
Logs of UV Imaging and X-Ray Observations of MCG-02-04-026

Facility	Band	λ/E[a]	Date	T_{exp}	Note
GALEX	FUV	1550 Å	2003 Oct 5	⋯	Pair1, pre-2014
GALEX	NUV	2340 Å	2003 Oct 5	⋯	
SDSS	u	3560 Å	2009 Oct 5	⋯	Pair2, pre-2014
SWIFT/UVOT	UVW2	2140 Å	2015 May 23	⋯	Pair1, post-2014
SWIFT/UVOT	U	3490 Å	2018 Jun 19	⋯	Pair2, post-2014
ROSAT/PSPC	X-ray	0.1–2.4 keV	1990	0.93 ks	
SWIFT/XRT	X-ray	0.3–8 keV	2015 May 23	2.4 ks	
SWIFT/XRT	X-ray	0.3–8 keV	2018 Jun 19	1.8 ks	

Note.
[a] The central wavelengths for UV filters and the available wavelength ranges for X-ray observations.

lamp spectra for the wavelength calibration for the blue and red sides, respectively. The standard star for flux calibration was observed about 1 hr before the observation of MCG-02-04-026. We reduced the data following a standard routine and extracted a spectrum in a 3″ aperture. For the TPSP observation, we used a slit with a 1″0 width, which resulted in a spectral resolution of 2000–2500. We used an A–B–B–A dithering mode to better remove the sky emission lines. The total exposure time was 40 minutes. We reduced the data and extracted a spectrum with the specX package.

2.4. Multiband Photometry for Spectral Energy Distribution

In order to generate the spectral energy distribution (SED) of MCG-02-04-026 before the MIR flare, we collected data observed by GALEX in 2003, by SDSS in 2009, by the Two Micron All Sky Survey (2MASS) in 1998, by WISE in 2010 (the first observation), by IRAS in 1983, and by the Very Large Array (VLA)/FIRST in 1997. We list the basic information of the observations in Table 5, including the facilities, the filters and their central wavelengths, and the dates. We aimed to get the integrated flux of the entire galaxy to avoid the influence of different spatial resolutions of images in different bands. For SDSS, 2MASS, IRAS, and VLA/FIRST observations, we collected the integrated fluxes of MCG-02-04-026 or corresponding magnitudes from public catalogs, which are described in detail in Table 5. And for GALEX and WISE observations, we measured the Petrosian aperture fluxes of the galaxy with SExtractor (v2.8.6, Bertin & Arnouts 1996). We also list the magnitudes/flux in Table 5.

3. Data Analysis

3.1. The MIR Flare

We generated the MIR LCs of MCG-02-04-026 over the 12 WISE observations using the PSF magnitudes in the $W1$ and $W2$ bands. We display the LCs in Figure 1(a). Before 2014, MCG-02-04-026's MIR radiation remained steady ($W1 \sim 11.00$ and $W2 \sim 10.46$). A rise of the radiation was captured by the seven observations during 2014 and 2017, indicating that there may be a flare in MCG-02-04-026. The radiation rose rapidly between 2014 January and July and kept rising to the peak ($W1 = 10.56 \pm 0.02$ and $W2 = 9.89 \pm 0.01$) in 2015 December. The radiation then dropped, and after 2017, it returned to the initial level with small variation.

We further confirmed the flare using an image subtraction technique. We did this using the WISE time-resolved co-added images from Meisner et al. (2018). In each of $W1$ and $W2$

bands, we created a pre-flare image by combining the images from the first three observations and a flare image by combining the images from seven observations during 2014 and 2017 July, and then we subtracted the pre-flare image from the flare image to obtain a residual image. We show these images in Figure 2. In the residual images, clearly excess radiations can be seen at the position of the galaxy, and meanwhile nearby objects show no significant excess radiations.

We measured the position of the flare by fitting the spatial brightness profile of the excess radiation with a two-dimensional Gaussian model. The results showed that the offsets between the position of the flare and the galaxy center are only 0.12 and 0.10 pixels[11] in the $W1$ and $W2$ bands, respectively. The errors to these offsets are dominated by systematic errors, which are at subpixel levels typically. So the position of the flare coincides with the galaxy center, and we can constrain their angular distance in 1 pixel and their projected distance in ~2 kpc in physical size. Besides, the flare behaved like a point source because the FWHM of the excess radiation (6″8 in $W1$ and 7″4 in $W2$) is consistent with those of nearby stars (6″1–7″1 in $W1$ and 6″5–7″5 in $W2$).

We measured the fluxes of the flare in each band of the seven observations between 2014 and 2017 July. We subtracted the pre-flare image that we obtained earlier from the co-added images in each band of each observation to get residual images. Then, we performed aperture photometry to the residual images. Except for the random error obtained in following the routine method of aperture photometry, there must also be a systematic error, which can be caused by a small position offset, PSF variation, and some other factors. In order to measure the systematic error, we made a test using several tens of nearby stars. We performed aperture photometry at the positions of the stars on the residual images. For each star, we calculated the rms of its fluxes on the seven residual images in each band. We found that the rms values of the stars are generally greater than the values predicted by random errors. So additional systematic errors, which are predicted to be ~3% of the stellar fluxes, are required to explain the rms values. Thus, for the flux of the flare, a systematic error of 3% of the flux of the galaxy nucleus measured in the pre-flare image was considered. The results, including the fluxes and the random and systematic errors, are listed in Table 6.

We generated the LCs and spectra of the flare, and we display them in Figures 3(a) and (b). The LC of the flare shows

---

[11] 1 pixel = 2″75 = 1.92 kpc.

Table 5
Photometric Data of MCG-02-04-026 to Construct a Pre-flare SED

Facility/filter	λ_c[a]	Mag/Flux	Date (UT)	Ref1[b]	Ref2[c]
GALEX/FUV	0.155 μm	18.85 ± 0.08 mag	2003 Oct 5	1	⋯
GALEX/NUV	0.234 μm	18.63 ± 0.04 mag	2003 Oct 5	1	⋯
SDSS/u	0.356 μm	17.42 ± 0.02 mag[d]	2009 Oct 5	2	3
SDSS/g	0.472 μm	15.687 ± 0.003 mag[d]	2009 Oct 5	2	3
SDSS/r	0.619 μm	14.807 ± 0.003 mag[d]	2009 Oct 5	2	3
SDSS/i	0.750 μm	14.320 ± 0.003 mag[d]	2009 Oct 5	2	3
SDSS/z	0.896 μm	13.901 ± 0.004 mag[d]	2009 Oct 5	2	3
2MASS/J	1.24 μm	12.61 ± 0.03 mag[e]	1998 Oct 30	4	5
2MASS/H	1.66 μm	11.77 ± 0.04 mag[e]	1998 Oct 30	4	5
2MASS/K	2.16 μm	11.31 ± 0.04 mag[e]	1998 Oct 30	4	5
WISE/W1	3.35 μm	10.64 ± 0.02 mag	2010 Jul 9	6	⋯
WISE/W2	4.60 μm	10.21 ± 0.02 mag	2010 Jul 9	6	⋯
WISE/W3	11.6 μm	6.87 ± 0.02 mag	2010 Jul 9	6	⋯
WISE/W4	22.1 μm	5.20 ± 0.03 mag	2010 Jul 9	6	⋯
IRAS/60 μm	61.5 μm	0.51 ± 0.05 Jy[f]	1983	7	8
IRAS/100 μm	102 μm	1.27 ± 0.13 Jy[f]	1983	7	8
VLA/L	21 cm	3.68 ± 0.16 mJy[g]	1997 Mar 2	9	10

Notes.

[a] The central wavelengths of the filters.

[b] The references for the facilities: (1) Martin et al. 2005; (2) York et al. 2000; (4) Skrutskie et al. 2006; (6) Wright et al. 2010; (7) Neugebauer et al. 1984; (9) Becker et al. 1995.

[c] The references for the magnitudes or fluxes: (3) Alam et al. 2015; (5) Jarrett et al. 2000; (8) Beichman et al. 1988; (10) Helfand et al. 2015. For GALEX and WISE, the magnitudes were measured from the images by us.

[d] The magnitudes resulting from modeling the galaxy's brightness profile (modelMag), which were collected from the SDSS photometric catalog from SDSS Data Release 12.

[e] The magnitudes measured in the "total" aperture defined in Jarrett et al. (2000), which were collected from the 2MASS extended source catalog.

[f] The flux densities from the IRAS point-source catalog.

[g] The integrated flux density from the VLA/FIRST source catalog.

a similar pattern to the LC of MCG-02-04-026. We saw a change in the spectral shape of the flare (Figure 3(b)). The change can be seen more clearly from the variation of the MIR color, which can be expressed as the ratio between the flare's fluxes in the $W1$ and $W2$ bands ($f_\lambda(W1)/f_\lambda(W2)$, smaller for redder), which is plotted in Figure 3(c). The MIR color of the flare was generally turning red.

We estimated the IR luminosity (L_{IR}) and the total IR energy (E_{IR}) of the flare as follows. First, because only the data in the $W1$ and $W2$ bands (their passbands are 2.8–3.8 μm and 4.0–5.3 μm, respectively) are available, we calculated the IR luminosity in the range of 2.8–5.3 μm ($L_{2.8-5.3\,\mu m}$) and considered it as the lower limit of L_{IR}. We fit the spectra of the flare with power-law models, which are expressed as

$$f_\nu(\lambda) = \begin{cases} C_1\lambda^{C_2}, & \lambda_1 < \lambda < \lambda_2 \\ 0, & \lambda < \lambda_1 \text{ or } \lambda > \lambda_2 \end{cases}, \quad (1)$$

where C_1 and C_2 are free parameters, and $\lambda_1 = 2.8\ \mu$m and $\lambda_2 = 5.3\ \mu$m. The $L_{2.8-5.3\,\mu m}$ inferred from the power-law models are shown in Figure 3(d). We obtained an energy of 7.4×10^{50} erg by integrating the $L_{2.8-5.3\,\mu m}$ curves over time. This value sets the lower limit of E_{IR}. Then, we estimate the L_{IR} using blackbody models, because the IR spectrum of a similar MIR flare, Arp 299-B AT1 (Mattila et al. 2018), conforms to the blackbody curve in a wider wavelength range (1.2–8 μm). The blackbody models are expressed as

$$f_\nu = \frac{\pi B_\nu(T_{BB})4\pi r_{BB}^2}{4\pi D_L^2}, \quad (2)$$

where T_{BB} (blackbody temperature) and r_{BB} (blackbody radius) are free parameters. The blackbody temperature (Figure 3(e)) was roughly dropping, corresponding to the variation in the spectral shape, and was about 1000 K most of the time. The blackbody radius (Figure 3(f)) was roughly increasing and reached a maximum value of ∼100 lt-day in 2016. Using blackbody models, we calculated blackbody luminosities (Figure 3(g)) and integrated them up to obtain a total energy of 1.8×10^{51} erg. Thus, the total IR energy E_{IR} exceeds ∼7×10^{50} erg and is likely to be on the order of 10^{51} erg.

3.2. No Detection of Variability in Optical and UV

We show the optical LCs of MCG-02-04-026 from CSS, PTF, and ASAS-SN in Figure 1(b). The mean magnitudes of the three LCs are different ($V_{CSS} = 14.75$ for CSS, $R = 14.85$ for PTF, and $V = 15.27$ for ASAS-SN), because the bands and apertures for photometry are different. We saw no internal variability in any of the three LCs. Thus, no optical flare corresponding to the MIR flare was recorded. The typical error levels, which are calculated from the rms of the errors for each LC, are 0.03, 0.05, and 0.04 mag for CSS, PTF, and ASAS-SN, respectively. Thus, any possible optical flare either fell into the gap between observations or had a variability amplitude lower than 0.1 mag.

We check possible UV variation by subtracting UV images taken before 2014 from those taken after 2014, the year when the MIR flare began. We used two pairs of images, each of which contains a pre-2014 image and a post-2014 image, as listed in Table 4. In the first pair, the post-2014 image was
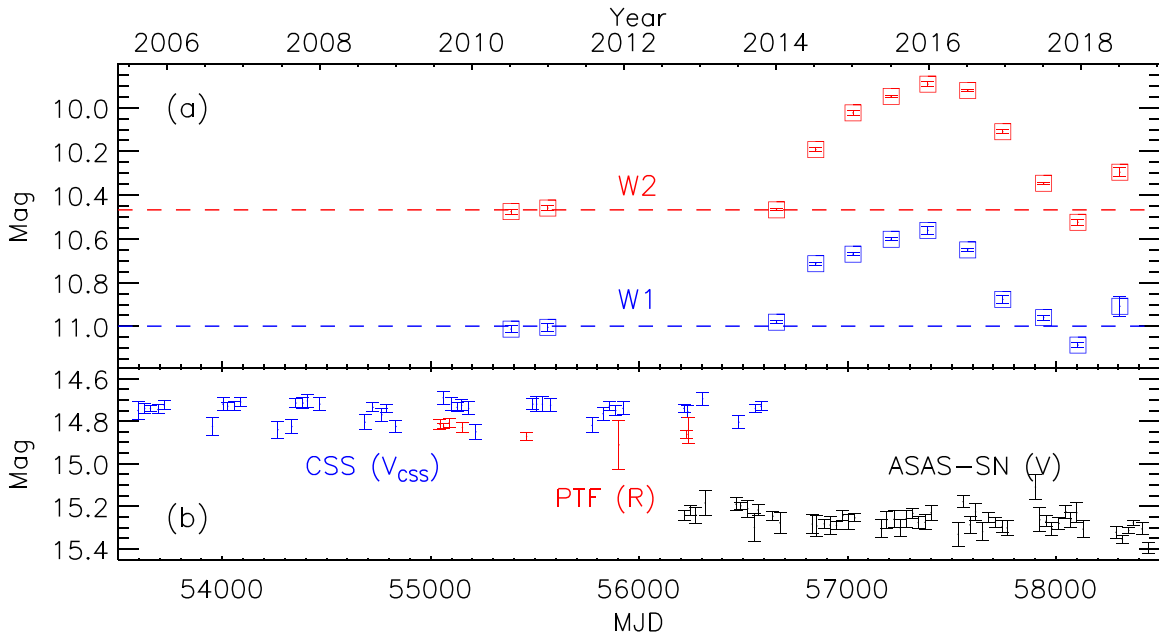
Figure 1. (a) MIR LCs of MCG-02-04-026 in *W*1 (red) and *W*2 (blue) bands. The LCs were constructed using PSF magnitudes. The horizontal dashed lines show the levels in the two bands before the flare. (b) Binned optical LCs from surveys of CSS (blue), PTF (red), and ASAS-SN (black).

taken by SWIFT/UVOT in 2015 with the UVW2 filter (central wavelength $\lambda_c = 2140$ Å), and the pre-2014 image was a fake image created using GALEX images taken in 2003 with the NUV ($\lambda_c = 2340$ Å) and FUV ($\lambda_c = 1550$ Å) filters. We created the fake image as follows: for each spatial pixel, we calculated the flux at 2140 Å by interpolating the fluxes at 2340 Å and at 1550 Å by assuming a spectral shape of a power law. In the second pair, the pre-2014 image was taken by SDSS in 2009 with the *u* filter ($\lambda_c = 3560$ Å), and the post-2014 image was taken in 2018 with the *U* filter ($\lambda_c = 3490$ Å). For each pair, the subtraction was done as follows: we first aligned the pair of images, then blurred the image with higher spatial resolution by convolving with a Gaussian to let it have the same spatial resolution with the other image, then multiplied one of the pairs by a constant factor, and finally performed subtraction. The pre-2014, post-2014, and residual images in the two pairs are shown in Figure 4. Neither of the residual images shows obvious excess radiation.

To conclude, neither optical nor the UV flare corresponding to the MIR flare was detected based on available data.

3.3. The Optical and NIR Spectral Properties and Possible Spectral Variations

We show the two optical spectra of MCG-02-04-026, including a spectrum taken with BOSS in 2013 November (hereafter Y2013) and a spectrum taken with DBSP in 2018 January (hereafter Y2018), in Figure 5(a). In both of the two spectra, the continua are dominated by starlight and prominent emission lines can be seen. To inspect possible spectral variation caused by the MIR flare, we calculated the ratio between the Y2018 and Y2013 spectra (Figure 5(b)). The ratio shows that the continuum varied little. A wavelength-independent variation with amplitude of ∼5% is possibly due to different apertures used when taking the two spectra (Figure 5(c)). The ratio also shows that the flux around Hα increased from 2013 to 2018, which we will explain later.

Since we were concerned with the emission lines, we modeled the starlight and subtracted them from the observed spectra to obtain emission-line spectra. We modeled the starlight using a linear combination of principal component templates of spectra of simple stellar populations (SSPs). We used the templates from Lu et al. (2006), which were built from the library of SSP spectra of Bruzual & Charlot (2003). We fit the starlight model to the two spectra in regions that are free of emission lines. In the fitting, the combination of the templates was shifted with a redshift parameter z(star), broadened by convolving with a Gaussian with a velocity dispersion parameter σ(star), and reddened by multiplying by the Milky Way's extinction curve of Fitzpatrick (1999) with a reddening parameter E_{B-V}(star). We plot the starlight models in Figure 5(a) and list the parameters in Table 7.

In Figure 6, we show the emission-line spectra from the Y2013 and Y2018 observations in two wavelength ranges; one is around Hβ+[O III], and the other is around Hα. In both of the two spectra, we detected Hα broad emission lines (BELs) and meanwhile detected no Hβ BELs. For each spectrum, we simultaneously modeled the Hα BELs and narrow emission lines (NELs), including Hβ, [O III] $\lambda\lambda 4959, 5007$, [O I] $\lambda 6300$, [N II] $\lambda\lambda 6548, 6583$, H$\alpha$, and [S II] $\lambda\lambda 6716, 6731$. In the model, H$\alpha$ BEL and all the NELs are assumed to have single Gaussian profiles. The centroids and widths in term of velocity of all the NELs are tied. The flux ratios of [N II] and [O III] doublet lines are fixed to be 3. We plotted the emission-line model in Figure 6 and listed the parameters in Table 7.

We can categorize MCG-02-04-026 as a Seyfert 1.9 galaxy according to the detection of Hα BELs and no detection of Hβ BELs. We can also categorize it as a low-ionization nuclear emission-line region (LINER) galaxy using the ratios of NELs, which are listed in Table 7, according to the diagnostic diagram of Kewley et al. (2006). The categorizations based on the two optical spectra are consistent and indicate that MCG-02-04-026 is an active galaxy. Note that there is a possible non-AGN interpretation of the BELs that the BELs might be newly generated by an event that caused the MIR flare. This was
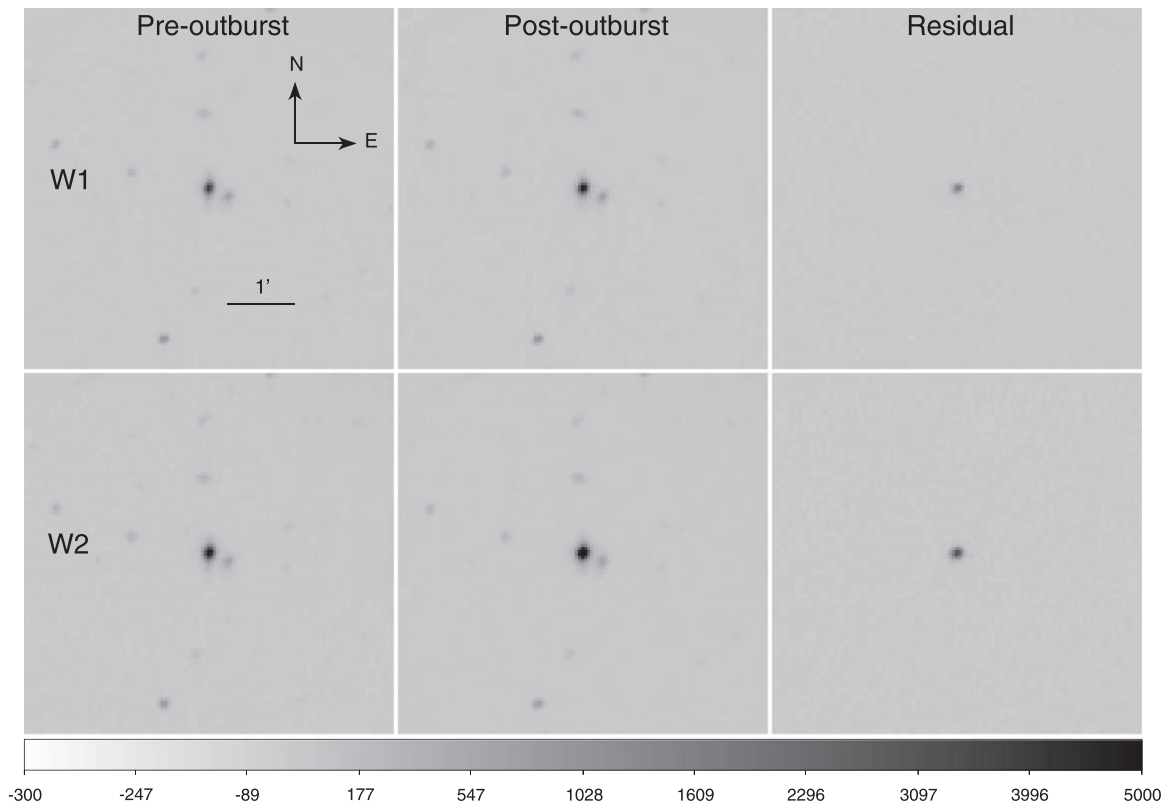
Figure 2. Pre-flare images (left panels), flare images (middle panels), and the residual images (right panels) by subtracting the pre-flare images from the flare images. We show the images in the W1 filter in the top panels and the images in the W2 filter in the bottom panels. The images are plotted in a uniform square-root scale, which is shown in the grayscale bar.

unlikely to happen, because the Y2013 observation was taken 1.5 months before the WISE observation in 2014 January, during which no MIR excess radiation was seen, and because the Y2018 observation was taken when the MIR flare had faded. Even if the BELs were not caused by an AGN, the narrow-line ratios like those of LINERs are evidence of MCG-02-04-026 being an active galaxy, because LINERs are usually related to AGNs (Ho 1999), and the narrow-line fluxes do not change in a short time.

The model shows that the flux of Hα BEL on the Y2018 spectrum increases for ∼30% relative to that on the Y2013 spectrum, and the profile of Hα BEL also varies. Such a variation is commonly seen in active galaxies, so we were not interested in this. The variation is consistent with the fact we found earlier that the flux around Hα increased from 2013 to 2018.

The NIR spectrum of MCG-02-04-026 (Figure 5(d)) is dominated by continuum. The only emission line that we can identify with certainty is Paβ BEL.[12] We modeled the local continuum around Paβ using a two-order polynomial (red line in Figure 5(d)) and show the emission-line spectrum after subtracting the continuum in the right panel of Figure 6. We also modeled the Paβ BEL using a single Gaussian and list the parameters in Table 7.

Generally there is dust on the line of sight to the nucleus of a Seyfert 1.9 galaxy, causing the reddening of the nuclear emission. We estimated the dust reddening to the nucleus of

MCG-02-04-026 by comparing the observed to the intrinsic flux ratios of the BELs. The flux ratios of Hα/Hβ and Hα/Paβ were used. Although Hβ BEL is not detected, we can estimate an upper limit of its flux and hence a lower limit of Hα/Hβ. The upper limit of Hβ BEL flux is estimated as follows. First, we added an Hβ BEL component of which the center and width in terms of velocity were tied to that of an Hα BEL, and we fit the emission-line spectrum again to obtain a random error. Next, we estimated the systematic error introduced when subtracting the continuum: we chose different wavelengths where no actual emission lines exist on the emission-line spectrum, supposed that there were hypothetical BELs at these wavelengths, measured the fluxes they would have, and estimated the systematic error by interpreting the rms of the fluxes. Then, we calculated a total error by combining the random error and the systematic error. Finally, we obtained a 3σ upper limit of the flux of the Hβ BEL. We list the upper limits from the two optical spectra in Table 7. We also list the observed flux ratios of Hα/Hβ and Hα/Paβ from Y2013 and Y2018 observations in Table 8. We adopted Case B values as the intrinsic flux ratios: an Hα/Hβ value of 2.72 (Gaskell 2017), and an Hα/Paβ value of 19 (Storey & Hummer 1995).[13] We estimated the nuclear dust reddening using three extinction curves, including a Milky Way one from Fitzpatrick (1999), an LMC averaged one from Misselt et al. (1999), and an SMC one from Pei (1992). The resultant E_{B-V} values are listed in Table 8. The E_{B-V} values inferred from the two flux ratios from the observations in 2018 are consistent,

---

[12] Notice that the Paα and Paγ+He I λ10830 emission lines, which are commonly seen in a Seyfert galaxy's spectrum, fall into regions strongly affected by telluric absorptions.

[13] We assumed that the broad-line region has an electron temperature $T_e = 15,000$ K and an electron density $n_e = 10^9$ cm^{-3}.

Table 6
Excess Fluxes in MIR and the Parameters of Blackbody Curves That Match Them

Date	MJD (days)	Phase (days)	$f_\nu W1$ (mJy)	$f_\nu W2$ (mJy)	$f_\nu W1/f_\nu W2$	T_{BB} (K)	r_{BB} (lt-day)	$L_{2.8-5.3\,\mu m}$ (10^{42} erg s^{-1})	L_{BB}
2014 Jul 9	56848	0	$3.71 \pm 0.13 \pm 0.36$	$3.56 \pm 0.13 \pm 0.33$	$1.03^{+0.17}_{-0.13}$	1400^{+370}_{-220}	28^{+8}_{-8}	5.7 ± 0.5	15^{+5}_{-3}
2015 Jan 4	57027	173	$4.92 \pm 0.14 \pm 0.36$	$5.65 \pm 0.22 \pm 0.33$	$0.87^{+0.11}_{-0.08}$	1140^{+170}_{-110}	48^{+10}_{-9}	8.0 ± 0.5	$18.4^{+2.1}_{-1.3}$
2015 Jul 6	57210	350	$5.32 \pm 0.13 \pm 0.36$	$7.68 \pm 0.14 \pm 0.33$	$0.69^{+0.06}_{-0.06}$	920^{+80}_{-60}	79^{+12}_{-11}	9.4 ± 0.5	$21.4^{+0.9}_{-0.9}$
2015 Dec 29	57386	520	$6.03 \pm 0.15 \pm 0.36$	$7.71 \pm 0.17 \pm 0.33$	$0.78^{+0.07}_{-0.06}$	1020^{+90}_{-70}	66^{+10}_{-9}	10.1 ± 0.5	$22.8^{+1.2}_{-1.0}$
2016 Jul 7	57577	704	$5.04 \pm 0.13 \pm 0.36$	$8.04 \pm 0.14 \pm 0.33$	$0.63^{+0.05}_{-0.05}$	850^{+60}_{-60}	95^{+15}_{-12}	9.3 ± 0.5	$22.0^{+1.0}_{-0.9}$
2016 Dec 22	57745	867	$2.04 \pm 0.13 \pm 0.36$	$4.56 \pm 0.13 \pm 0.33$	$0.45^{+0.09}_{-0.09}$	680^{+80}_{-80}	120^{+50}_{-30}	4.4 ± 0.4	$13.4^{+2.5}_{-1.5}$
2017 Jul 6	57941	1056	$1.11 \pm 0.13 \pm 0.36$	$2.11 \pm 0.11 \pm 0.33$	$0.54^{+0.23}_{-0.21}$	760^{+250}_{-190}	60^{+70}_{-30}	2.2 ± 0.4	$6.3^{+2.1}_{-1.1}$

and finally we adopted an E_{B-V} value from the Hα/Paβ flux ratio. The E_{B-V} value from the observations in 2018 meets with the lower limit set by the observation in 2013. Thus, there is no evidence that the nuclear dust reddening varied between 2013 and 2018.

3.4. The X-Ray Properties and Variations

We extracted X-ray images around MCG-02-04-026 using data from ROSAT 1991, SWIFT 2015, and SWIFT 2018 observations. We extracted in a range of 0.1–2.4 keV for ROSAT data and in a range of 0.3–8 keV for SWIFT data. The images are shown in Figure 7(a). We labeled the position of MCG-02-04-026 with red circles with radii of 1 'arcmin'. Note that there is another X-ray source, SDSS J012047.53-082629.5, which is a Seyfert 1 galaxy at $z = 0.230$, 3 'arcmin' north to MCG-02-04-026 (labeled with blue circles). The X-ray radiations from the two galaxies are blended in ROSAT data owing to the poor spatial resolution, leading to a large uncertainty of the flux of MCG-02-04-026 in 1991. Thus, we only analyzed the data from the two SWIFT observations taken in 2015 and 2018 hereafter.

The net count rate in 0.3–8 keV reduced from $(3.9 \pm 0.4) \times 10^{-2}$ counts s^{-1} in 2015 to $(1.6 \pm 0.3) \times 10^{-2}$ counts s^{-1} in 2018, indicating a significant (4.6σ) variation (a factor of 2.4 ± 0.5) in X-ray radiation of the galaxy. For a further check on the variation, we extracted spectra from the two observations. We show the two spectra in Figure 7(b), which were binned so that the data had at least 5 counts per bin. We fit the X-ray spectra with *XSPEC* (Version 12.9.0) with *C*-statistics adopted. In the fitting we considered the absorption from neutral gas in the Milky Way with $N_H = 3.8 \times 10^{20}$ cm^{-2} (Kalberla et al. 2005). Simple absorbed power-law models can fit both of the spectra. The models have three parameters: a photon index (Γ), an absorbing hydrogen column density (N_H), and an intrinsic 2–10 keV luminosity $L_{2-10\,keV}$. We list the parameters in Table 9. The Γ and N_H for the two spectra cannot be distinguished statistically. Because no change in Γ or N_H was seen, we interpreted the variation in the net count rate as the variation in the X-ray luminosity. Thus, we refit the two spectra by tying Γ and N_H. The intrinsic 2–10 keV luminosities $L_{2-10\,keV}$ are several $\times 10^{42}$ erg s^{-1} in both observations. The luminosities follow the correlation between X-ray and Hα luminosities for Seyfert galaxies (e.g., Panessa et al. 2006). While the luminosities of MCG-02-04-026 are higher than the typical values of star-forming galaxies (e.g., Mineo et al. 2014) and ultraluminous X-ray sources (e.g., Stobbart et al. 2006). Thus, the X-ray radiation in MCG-02-04-026 can be related to the AGN. However, there is also a possibility that the X-ray radiation could be generated by the event that caused the MIR flare, because both of the observations were taken after the MIR flare began. Besides, the hydrogen column density $N_H = (2.2 \pm 0.6) \times 10^{22}$ cm^{-2} falls between the typical values of Seyfert 1 and Seyfert 2 galaxies and is consistent with those of Seyfert 1.9 galaxies (e.g., Koss et al. 2017).

3.5. Pre-flare Spectral Energy Distribution

In Section 2.4, we generated a pre-flare SED of MCG-02-04-026 using photometric data taken before 2014. We show the SED in UV to far-IR (FIR) bands in Figure 8(a). The energy radiated by the galaxy is mainly in two wavelength ranges: one is the optical and NIR bands, and the other is the FIR band. This is in line with disk galaxies with recent star formation. We first fit the SED with a simple stellar radiation model. We fit it with a Python Code Investigating GALaxy Emission (CIGALE; Boquien et al. 2019), in which the radiation from stars and AGNs, the dust attenuation, and dust radiation are considered simultaneously by assuming an energy balance. We assumed that the stellar radiation consists of two components: one is starlight that is attenuated by dust, and the other is radiation of dust heated by stars. We assumed a delayed star formation history expressed as Equation (4) in Boquien et al. (2019) with three free parameters, including an age t_0, the time at which the star formation rate (SFR) peaks τ, and a normalization. Using these parameters, a stellar mass M_{star} and an SFR can be inferred. We used the SSP templates of Bruzual & Charlot (2003) and assumed an initial mass function described in Salpeter (1955) and a metallicity of 0.02. We selected the dust attenuation law described in Charlot & Fall (2000), with one free parameter that describes the *V*-band attenuation for the interstellar medium (ISM), A_V(ISM). We used dust emission templates provided by Dale et al. (2014) with one free parameter α. The simple stellar radiation model is shown in Figure 8(a). The model can fit the SED in optical, NIR, and FIR bands. However, the model is lower than the observed SED in UV and MIR bands, indicating excess radiations in the SED relative to a simple stellar radiation model.

We then explored the nature of the excess radiation in the UV band. We checked the GALEX images (Figure 4) and found that a large fraction of the UV flux comes from the outer region of the galaxy. The UV radiation is more extended than the optical radiation. The case is similar to the so-called "extended UV disks" (XUV disks; e.g., Gil de Paz et al. 2005). After visually inspecting the images, we found that the radiation of the XUV disk contributes to almost all of the galaxy's flux in the FUV band, a large fraction of flux in the NUV band, a small fraction of flux in the *u* band, and
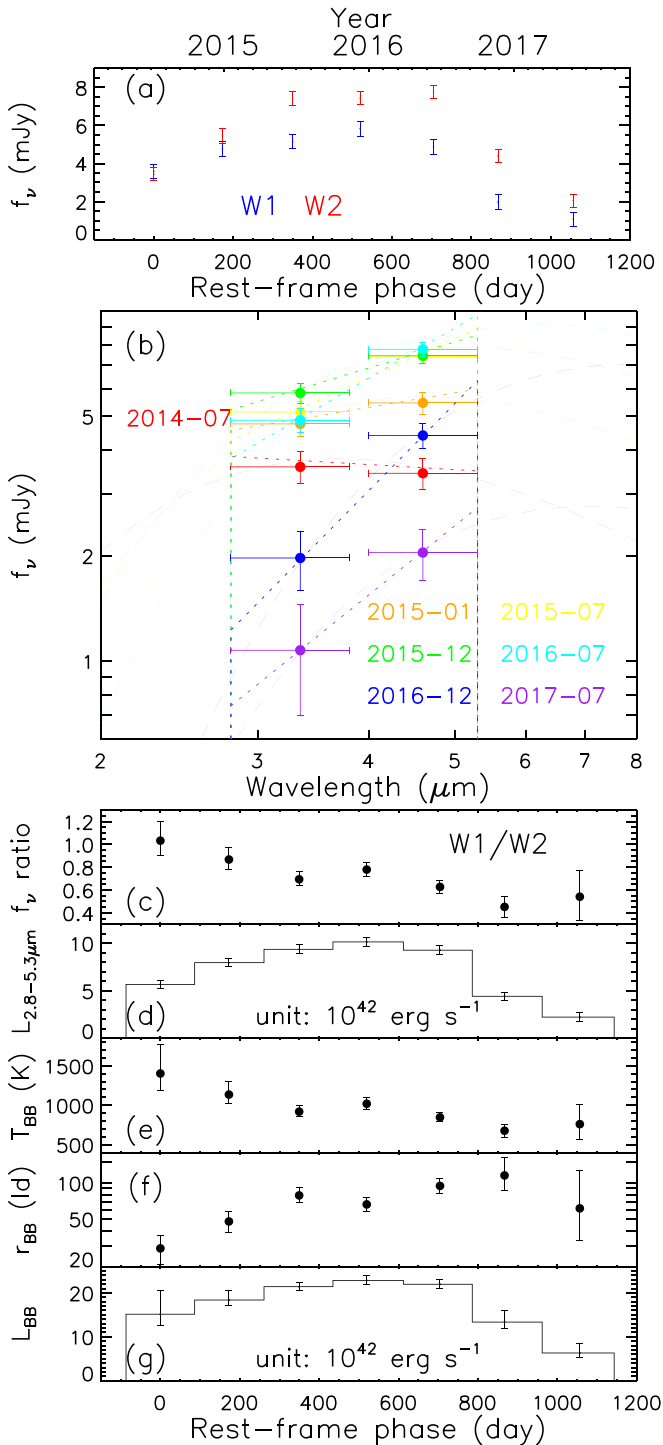
Figure 3. (a) LC of the MIR flare in the W1 and W2 bands during 2014 and 2017 July. The phase was calculated relative to the time of the first excess (MJD = 56,848) and was converted to the rest frame. (b) Spectra of the flare (data points), the power-law models (dotted lines), and the blackbody models (dashed lines). (c) MIR color expressed as the ratio between fluxes in the W1 and W2 bands. (d) IR luminosity in the wavelength range of 2.8–5.3 μm. (e, f) Blackbody temperature and blackbody radius. (g) Luminosity calculated using blackbody models.

negligible flux in bands with longer wavelengths. So we decomposed the radiation of the galaxy by assuming that it comes from two components, an XUV-disk component and a main-body component. We decomposed it with the code TPHOT (Merlin et al. 2016). We assumed that all the galaxy's

flux in the FUV band comes from the XUV-disk component, that all the flux in the g band comes from the main-body component, and that the fluxes in the NUV and u bands come from both components. We also assumed that the brightness profiles of each component in different bands are the same. The results show that the XUV-disk component contributes 50% and 14% of the fluxes in NUV and u bands, respectively. We fit the SED of the XUV-disk component (magenta pentagram in Figure 8(b)) in FUV to u bands with one other simple stellar radiation model. The model is shown with a cyan line in Figure 8(b), and the parameters are listed in Table 10. The dust extinction of the XUV-disk component is little, and the corresponding dust radiation is negligible. Using the model, we obtained the SFR in the XUV-disk component to be $0.5 \pm 0.1 \, M_\odot \, \mathrm{yr}^{-1}$.

We built an SED of the main-body component in NUV to FIR bands. The simple stellar radiation model cannot fit the SED, as the χ^2/dof is 33/10, and the excess radiation in the MIR bands still cannot be explained. Excess radiation in the MIR band can be related to the radiation of dust heated by AGNs. Thus, we added an AGN component in the model. We chose AGN templates from Fritz et al. (2006), which are suitable for the radiation of obscured AGNs. We fixed some parameters as described in Table 10, leaving three free parameters of the component, including the optical depth (τ) at 9.7 μm, the angle (ψ) between the AGN axis and the line of sight, and a normalization. An AGN luminosity can be inferred from the component. After adding this AGN component, the model fit the data, as χ^2/dof is 6.6/7. We show the model and its components in Figure 8(b) and list the parameters in Table 10. We obtained an SFR in the main-body component of $2.8 \pm 0.3 \, M_\odot \, \mathrm{yr}^{-1}$ and an AGN luminosity (L_{AGN}) of $(3.5 \pm 0.6) \times 10^{43} \, \mathrm{erg \, s}^{-1}$. After combining the SFRs in the two components, we estimated the total SFR of MCG-02-04-026 to be $3.3 \pm 0.3 \, M_\odot \, \mathrm{yr}^{-1}$.

The VLA flux at 1.4 GHz is 3.6 mJy, corresponding to a radio power of $1.1 \times 10^{22} \, \mathrm{W \, Hz}^{-1}$. Using the SED model from CIGALE, we calculated the 8–1000 μm luminosity of the galaxy to be $5 \times 10^{10} \, L_\odot$. The radio power and the 8–1000 μm luminosity of MCG-02-04-026 follow the radio–IR correlation from Bell (2003) for inactive galaxies, and hence the AGN's contribution to the radio radiation is unnecessary.

3.6. The AGN Nature

There are three pieces of evidence of an AGN in MCG-02-04-026 before the MIR flare, including the Hα BEL in the optical spectrum taken in 2013, the narrow-line ratios that resemble those of LINERs, and the MIR excess in the pre-flare SED relative to the stellar radiation model. After the MIR flare faded in 2017, both the BELs in the optical and NIR spectra taken in 2018 and the luminous ($L_{2-10 \, \mathrm{keV}} > 10^{42} \, \mathrm{erg \, s}^{-1}$) X-ray radiation in 2018 suggest that the nuclear activity was continuing, though we cannot rule out the possibility that these could be caused by the event that produced the MIR flare. The radio radiation of MCG-02-04-026 is weak and can have a stellar origin, so the AGN is radio-quiet.

The nuclear emission of MCG-02-04-026 is partially obscured because the BELs are reddened by dust and X-ray radiation is absorbed by gas. We saw no evidence of variations of dust reddening and gas absorption. Thus, we considered them as invariable and adopted a dust reddening (E_{B-V}) of 1.3–1.8, and hence an extinction (A_V) of 4.4–5.0, depending on
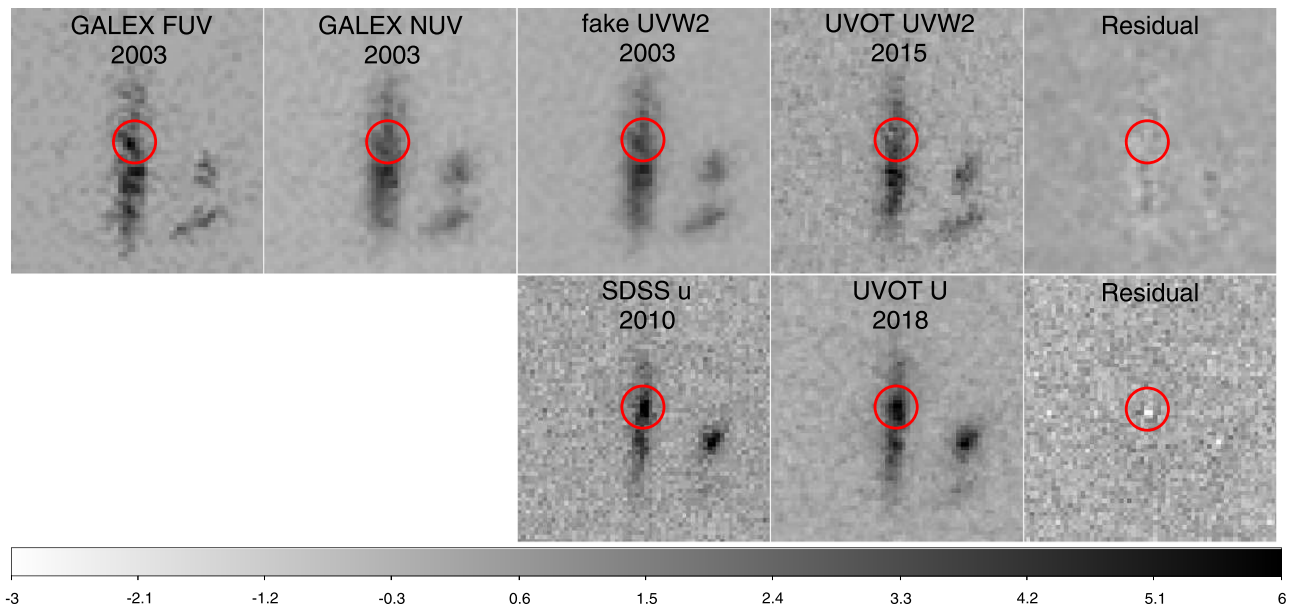
Figure 4. Pre-2014, post-2014, and residual images in the two pairs of UV images. Those in the first pair are shown in the top row, and those in the second pair are shown in the bottom row. We show the pre-2014 images in the third column, post-2014 images in the fourth column, and residual images in the fifth column. We also show the two GALEX images from which the pre-2014 image was obtained in the first and second columns in the top row. For each image, we labeled which facility and filter were used in the observation, as well as the year of the observation. We also labeled the center of the galaxy using red circles with radii of 5″. All the images are normalized and are plotted in a uniform linear scale, which is shown in the grayscale bar.

the choice of extinction curves, and a hydrogen column density (N_{H}) of 2.2×10^{22} cm^{-2}.

We had obtained an AGN bolometric luminosity (L_{AGN}) value of $10^{43.5}$ erg s^{-1} after modeling the pre-flare SED in the optical–IR bands. The L_{AGN} can also be estimated using X-ray luminosity $L_{2-10\,\mathrm{keV}}$. We chose the X-ray luminosity from the observation in 2018, because it was likely less affected by the event that caused the MIR flare, and adopted a bolometric correction of $\sim$20 from Hopkins et al. (2007). We thus obtained one other L_{AGN} value of $10^{43.7}$ erg s^{-1}. The two values are close, and hence we adopted the mean value of $L_{\mathrm{AGN}} \sim 10^{43.6}$ erg s^{-1} as the final value.

We estimated the mass of the central SMBH M_{BH} using the relation between the M_{BH} and the FWHM and luminosity of Hα BEL (Greene & Ho 2005). The relation has an intrinsic scatter of 0.3 dex. Because the AGN is partially obscured, a correction for dust extinction must be made when using the observed Hα luminosity. We estimated a correction factor to be 20–50, depending on the choice of extinction curves. We calculated the M_{BH} using the two optical spectra separately. The two values are consistent, and we obtained an M_{BH} of $\sim 10^{7.0 \pm 0.4} M_{\odot}$. Note that the intrinsic scatter has been considered when calculating the error.

4. The Nature of the MIR Flare

In this section we discuss the nature of the MIR flare in MCG-02-04-026. We will interpret the observations of the flare with a dust echo model in Section 4.1 and discuss other possibilities in Section 4.2.

4.1. Dust Echo of a Primary Transient Event

Following some previous works on MIR flares in other galaxies (e.g., Jiang et al. 2017), we explore a possible scenario that the MIR flare in MCG-02-04-026 is the thermal reradiation from dust heated by UV–optical photons (i.e., dust echo) of a

primary nuclear transient event. Based on this scenario, we generated models of radiation of the dust echo by simulating the process, and during the simulation radiative transfer was involved. We generated models in different situations with different parameters and selected the optimal set of parameters so that the model fit the observations.

4.1.1. A Brief Introduction to the Model

Our model was based on the model of Lu et al. (2016, hereafter Lu16). Briefly, Lu16's model considered a point source and the dust around the point source. The point source was assumed to have a UV–optical luminosity $L(t)$ as a function of time t. The dust was assumed to have a spherically symmetric structure. And the dust grains have the same initial radius a_0 and are uniformly distributed with number density n_d, spanning from inner radius R_{in} to outer radius R_{out}. When the UV–optical radiation of the transient event arrives at the inner surface of the dust structure, it heats, sublimates, and destroys the dust grains there quickly. After the radiation fully sublimates the innermost dust grains, it continues to sublimate the dust grains in the outer layers that have lost "protection." The process goes on, eventually stopping at a distance of R_{sub} as the UV–optical radiation drops, and the outer dust grains can survive. The UV–optical radiation is converted to IR reradiation by the dust grains it heats up. The IR reradiation is attenuated by dust it passes through before it is finally received by the observer. In addition, due to a so-called light-travel time effect, the LC of the IR reradiation received by the observer is reshaped. The effect causes a time delay of the IR reradiation relative to the UV–optical radiation because the light-travel path of IR reradiation is longer than that of UV–optical radiation. The effect also elongates the time duration of the IR reradiation because of a difference in the lengths of the light-travel paths of IR reradiations from dust grains at different positions.
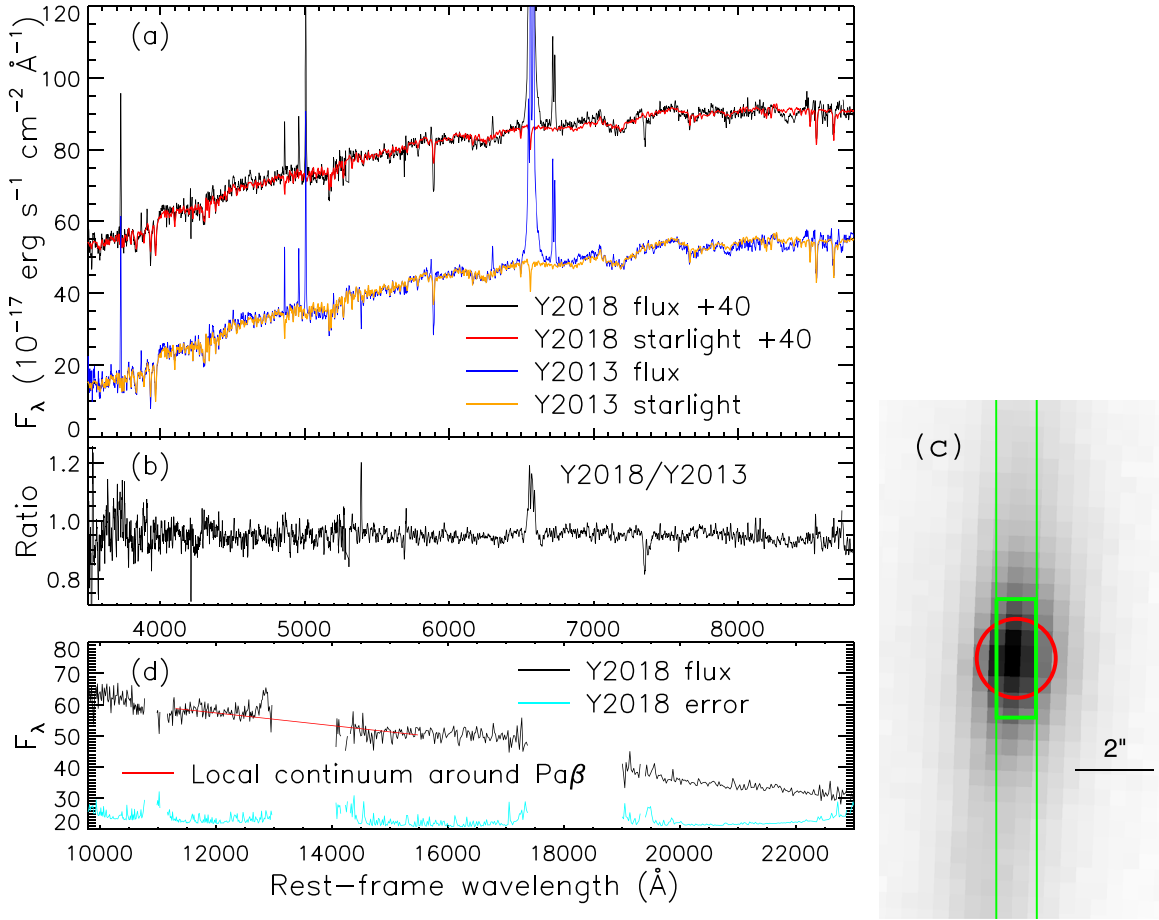
Figure 5. (a) Optical spectra taken in 2013 (blue) and in 2018 (black), and the starlight models for them (orange for Y2013 and red for Y2018). (b) Ratio between Y2018 and Y2013 spectra. (c) Aperture (red circle) used in the Y2013 observation with BOSS, and the slit and aperture (green lines) used in the Y2018 observation with DBSP. (d) NIR spectrum (black for flux and cyan for error) taken in 2018 with TPSP, and the local continuum model for the region around the Paβ emission line. Here we displayed the binned spectrum in regions little affected by telluric absorptions for clarity.

There are three differences between our model and Lu16's model. First, Lu16 assumed a constant UV–optical radiation during the3 transient event, and hence the UV_optical LV has a flat form, which is expressed as

$$\text{FLAT form:} \quad L(t) = \begin{cases} L_{\max}, & t_0 < t < \tau, \\ 0, & t < t_0 \vee t > \tau, \end{cases} \quad (3)$$

while we considered two more forms, including a TDE form and an EXP form expressed as

$$\text{TDE form:} \quad L(t) = \begin{cases} L_{\max}\left(1 + \dfrac{t - t_0}{\tau}\right)^{-5/3}, & t > t_0 \\ 0, & t < t_0 \end{cases} \quad (4)$$

$$\text{EXP form:} \quad L(t) = \begin{cases} L_{\max}\, e^{-t/\tau}, & t > t_0 \\ 0, & t < t_0. \end{cases} \quad (5)$$

Second, we used approximate empirical formulae to calculate the variation of some physical quantities in the simulation. These empirical formulae were obtained from results of rigorous simulations, and we will explain them in detail in the Appendix. Using empirical formulae greatly reduces the computation time required to generate a model, while ensuring validity of the results. Third, we set R_{sub} as a free parameter in the model. The first reason is that the R_{sub} values obtained from

the simulations may deviate from the reality, because there are too many parameters affecting R_{sub}, especially because some of the parameters, such as dust chemical properties, are not fully considered in the model. The second reason is that the R_{sub} parameter has a great influence on the shape of the final MIR LCs. In addition, the introduction of empirical formulae allowed us to set R_{sub} as a free parameter.

4.1.2. Fit to the Data

We fit the IR data of the MIR flare in MCG-02-04-026 with the simulations. We calculated a total energy of the UV–optical radiation $E_{\text{tot}} = \int_{t_0}^{\infty} L(t)\,dt$ and set t_0, $L_{\max}$, and E_{tot} as free parameters. We assumed a 1:1 mixture of graphite and silicate and used IR absorption coefficient data from Draine & Lee (1984). We tried four values of initial radius of grains (a_0) of 0.05, 0.10, 0.15, and 0.20 μm. We fixed the value of R_{in} to be the sublimation radius corresponding to the AGN luminosity $L_{\text{AGN}} \sim 10^{43.6}$ erg s^{-1} using the relation from Peterson (1997):

$$R_{\text{in}} = 0.4 \times \left(\frac{L_{\text{AGN}}}{10^{45}\ \text{erg s}^{-1}}\right)^{1/2} \text{pc}. \quad (6)$$

Thus, R_{in} is about 100 lt-day. We set R_{sub}, R_{out}, and n_d as free parameters. Finally, the model has six free parameters,

Table 7
Parameters for Modeling the Optical and NIR Spectra

Parameter	2013	2018
Starlight		
z(star)	0.03485 ± 0.00002	0.03485 ± 0.00003
σ(star)	90 ± 5	130 ± 10
E_{B-V}(star)	0.31 ± 0.01	0.30 ± 0.01
BEL		
Hα velocity	460 ± 10	363 ± 8
Hα FWHM	2500 ± 20	2230 ± 15
Hα flux	2250 ± 20	2920 ± 30
Paβ velocity	$\cdots$	550 ± 140
Paβ FWHM	$\cdots$	3100 ± 300
Paβ flux	$\cdots$	1230 ± 110
Hβ flux	<160	<220
NEL		
Velocity	-50 ± 1	-51 ± 1
FWHM	288 ± 2	326 ± 3
Hβ	127 ± 3	108 ± 7
[O III] $\lambda5007$	348 ± 5	341 ± 7
[O I] $\lambda6300$	66 ± 3	51 ± 5
Hα	724 ± 9	687 ± 11
[N II] $\lambda6583$	675 ± 9	661 ± 10
[S II] $\lambda6716$	246 ± 4	227 ± 5
[S II] $\lambda6731$	193 ± 4	185 ± 5
NEL Ratio		
[O III]/Hβ	2.74 ± 0.07	3.16 ± 0.20
[N II]/Hα	0.93 ± 0.02	0.96 ± 0.02
[S II]/Hα	0.61 ± 0.01	0.60 ± 0.01
[O I]/Hα	0.091 ± 0.004	0.074 ± 0.007

Note. All the velocities, velocity dispersions, and FWHMs are in units of km s^{-1}. All the fluxes are in units of 10^{-17} erg s^{-1} cm^{-2}.

including t_0, $L_{\max}$, E_{tot}, R_{sub}, R_{out}, and n_d, and a multiselection parameter a_0 (four selections).

For each form of the UV–optical LC, we derived the parameters by minimizing χ^2. The overall minimum χ^2 (10.8 for 8 degrees of freedom) was obtained when the UV–optical LC has a TDE form, and the parameters are $a_0 = 0.15 \, \mu$m, t_0(MJD) $= 56740 \pm 30$, $E_{\text{tot}} = 9^{+4}_{-2} \times 10^{51}$ erg, $L_{\max} = 5^{+3}_{-2} \times 10^{44}$ erg s^{-1}, $R_{\text{sub}} = 370 \pm 20$ lt-day, $R_{\text{out}} = 600^{+400}_{-200}$ lt-day, and $n_d = 6^{+20}_{-3} \times 10^{-9}$ cm^{-3}. We show the model yielding the overall minimum χ^2 in Figure 9 by plotting the UV–optical LC of the primary transient event in Figure 9(a) and plotting the MIR LCs of the dust echo in Figure 9(b). As can be seen in Figure 9(b), the model reproduces the observation of the MIR flare.

The model predicted that the primary transient event reached its peak luminosity around 2014 March. However, the optical V-band LC data from ASAS-SN observations taken around this time show no optical flares. As the nuclear region of MCG-02-04-026 is severely obscured by dust with $A_V = 4.4$–5.0, we checked whether the nondetection of optical variation can be explained by dust obscuration. We generated V-band LC models by assuming that the SED of the UV–optical radiation of the primary transient event is a blackbody curve with a temperature of 1.7×10^4 K, which is the temperature value of PS16dtm when its optical luminosity was around the peak level

(Blanchard et al. 2017). We generated two models, one with no obscuration and the other with an obscuration of $A_V = 4.7$. We show the two models in Figure 9(c). The models show that the transient event might cause a V-band magnitude variation of >1 if there were no obscuration, while it could only result in a variation of $\sim$0.04 under a severe dust obscuration. We had obtained an error level of the V-band magnitude of MCG-02-04-026 from ASAS-SN to be $\sigma = 0.04$ mag. Thus, the predicted V-band magnitude variation is below the 3σ detection level. Therefore, the dust obscuration can explain the nondetection of optical variation. The dust obscuration can also explain the nondetection of variation in the UV band, where extinction is greater.

4.1.3. Constraints to the Form of UV–Optical LCs

We list the fitting results by using UV–optical LCs with each of the three forms in Table 11. We found that the fits using TDE-form and EXP-form UV–optical LCs are much better than fits using FLAT-form UV–optical LCs. To show this clearly, we display the best-fitting models with the three forms of UV–optical LCs in Figure 10. Although the model using UV–optical LCs with the FLAT form can give MIR LCs with shapes roughly matching the observation, it cannot reproduce the observed variation in the MIR color at the same time, as can be seen in Figure 10(d). Thus, the data seem to support UV–optical LCs that decrease soon (no more than several months) after reaching the peak, rather than UV–optical LCs with plateaus whose time duration is as long as $\sim$1 yr.

We should note that our dust echo model assumed a fast-evolving transient event during which the UV–optical radiation peaks in a short timescale. Under this assumption, most of the energy of the UV–optical radiation is released in a short time, and the shape of the MIR LC is roughly determined by the light-travel time effect. Another possible model is that the MIR flare could be caused by a slowly evolving transient event whose UV–optical LC has a similar shape to the observed MIR LC. We checked this possible model using a simulation. The simulation was similar to the simulation described in Section 4.1.1, except that we assumed a slowly evolving transient event whose UV–optical LC is shown with a red line in Figure 10(a), and except that we set the inner radius of the dust structure as a constant. The latter assumption is because it is not necessary to consider the change in the inner radius of the dust due to sublimation when the peak luminosity of the transient event is close to the AGN luminosity, as argued by Almeyda et al. (2017).[14] We show the MIR LCs and the variation in the MIR color of the dust echo radiation in the simulation in Figures 10(b)–(d). We compared them with those of dust echo radiations produced by fast-evolving transient events with TDE-form and EXP-form UV–optical LCs. The shapes of MIR LCs are similar; however, the variations in the MIR color are completely different. The dust echo radiation produced by a slowly evolving transient event turns blue as it rises and turns red as it drops, while the dust echo radiation produced by a fast-evolving transient event keeps turning red both when it rises and when it drops. The latter is consistent with the observation. Therefore, the MIR flare in MCG-02-04-26 was produced by a fast-evolving transient event rather than a slowly evolving one.
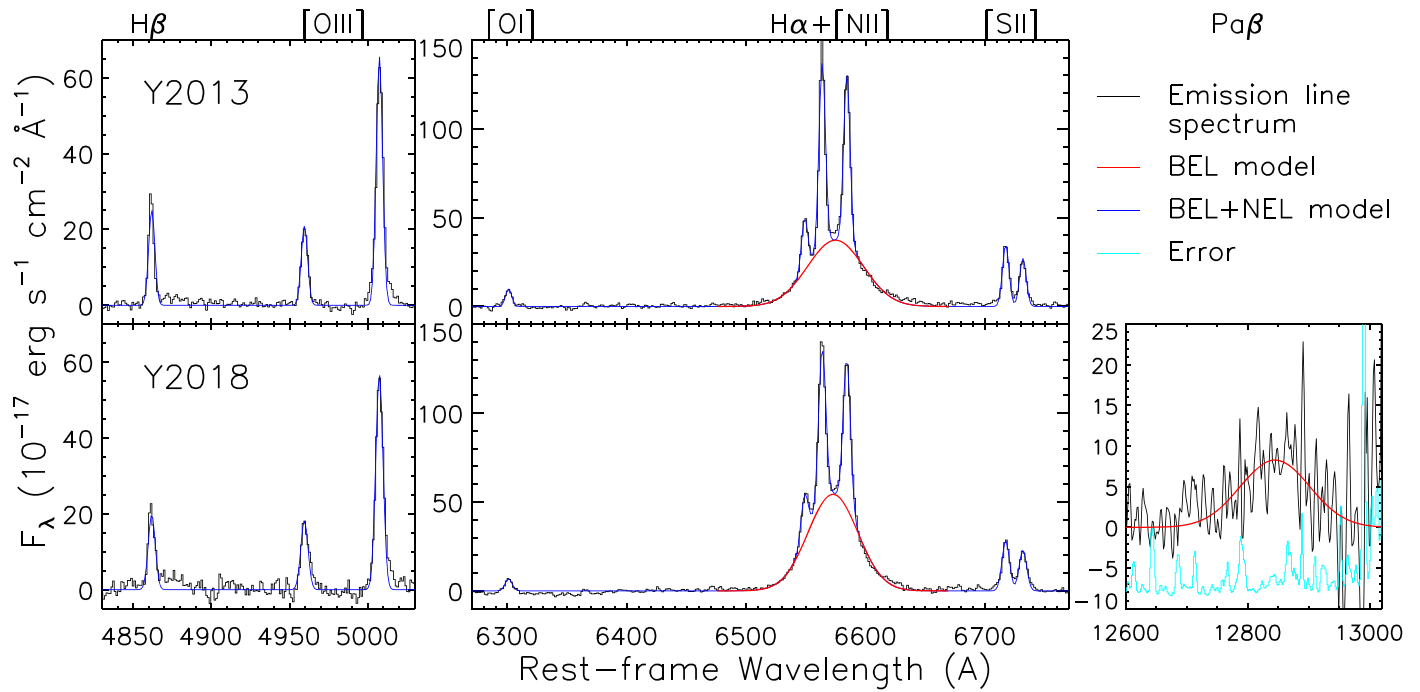
---

[14] In their Section 2.5.

Figure 6. Emission-line spectra (black) from Y2013 (top panels) and Y2018 (bottom panels) observations and the models (blue), displayed in three wavelength ranges; the first is around Hβ+[O III] (left panels), the second is around Hα (middle panels), and the third is around Paβ (right panel). The models contain BEL components and NEL components, and we show the BEL components with red lines. We also show the error of the NIR spectrum (minus 10) with the cyan line.

Table 8
Reddening to the BELs

Parameter		2013	2018
Hα/Hβ	Observed	>14.1	>13.3
	Intrinsic	2.72	
	Ratio	>5.2	>4.9
Hα/Paβ	Observed	...	2.4 ± 0.2
	Intrinsic	19	
	Ratio	...	0.12 ± 0.01
E_{B-V}	MW	>1.4	1.37 ± 0.06[a]
	LMC average	>1.4	1.25 ± 0.05[a]
	SMC	>1.8	1.78 ± 0.07[a]

Note.
[a] The values converted from Hα/Paβ flux ratios are adopted.

4.2. Other Possibilities

The MIR flare in MCG-02-04-026 is unlikely to be nonthermal radiation from a relativistic jet that is amplified by the beaming effect like those in blazers (e.g., Jiang et al. 2012), because the galaxy is radio-quiet, and because we saw no dramatic variability on timescale of hours to days. Thus, it must originate from thermal radiation from dust, which was heated by energy released in a primary transient event.

The dust can be heated by radiation or by shock. Here we discuss whether the dust can be heated by shock or not. The shock may be produced by a wind or a jet that collides with gas surrounding the dust. Here the wind refers to slow and scattered gas flow, and the jet refers to fast (close to the speed of light) and concentrated gas flow. We first considered the case of the wind. There are two facts. One is that the blackbody radius of the MIR flare radiation goes up to ∼100 lt-day, indicating that the IR radiating dust is distributed in a vast space. The other is that most of the IR energy was released in 3–4 yr, indicating

that the wind interacts with the IR radiating dust in different positions in a shorter time. These two facts required that the velocity of the wind must be at least ∼0.1c. The ejecta of SNe or the outflows of TDEs may have such a high velocity in their early stages, but they will slow down to ∼0.01c or lower velocities after expanding to larger space. Thus, it is unlikely that the dust is heated by shock produced by wind. We then considered the case of the jet. In this case, the IR energy comes from the kinetic energy of the jet. From the observed IR luminosity, it can be estimated that the power of the jet exceeds 2×10^{36} W. Considering that the kinetic energy is not completely converted into thermal energy, the power of the jet needs to be higher. Such a powerful jet would only been seen in radio galaxies (e.g., Merloni & Heinz 2007). MCG-02-04-026 is not a radio galaxy. Thus, it is unlikely that the dust is heated by a shock produced by a jet either.

Therefore, we concluded that the MIR flare is the dust echo of a primary transient event.

5. The Origin of the Primary Transient Event

Although the primary transient event was not seen directly owing to dust obscuration, we can estimate its timescale and energy budget. Most of the IR energy was released during ∼3 yr. Because the light-travel time effect elongates the duration of dust echo radiation, the energy release timescale of the primary transient event that caused the MIR flare must be shorter. Therefore, even the most conservative consideration can limit the energy release timescale to be less than ∼3 yr. We had obtained a total IR energy E_{IR} to be at least ∼10^{51} erg. Because not all of UV photons can be absorbed by dust and then reprocessed into IR photons, E_{IR} set a lower limit of the total energy of the primary transient event E_{tot}.

On the nature of the primary transient event, we can rule out the possibility of normal SNe (that means not SLSNe) because
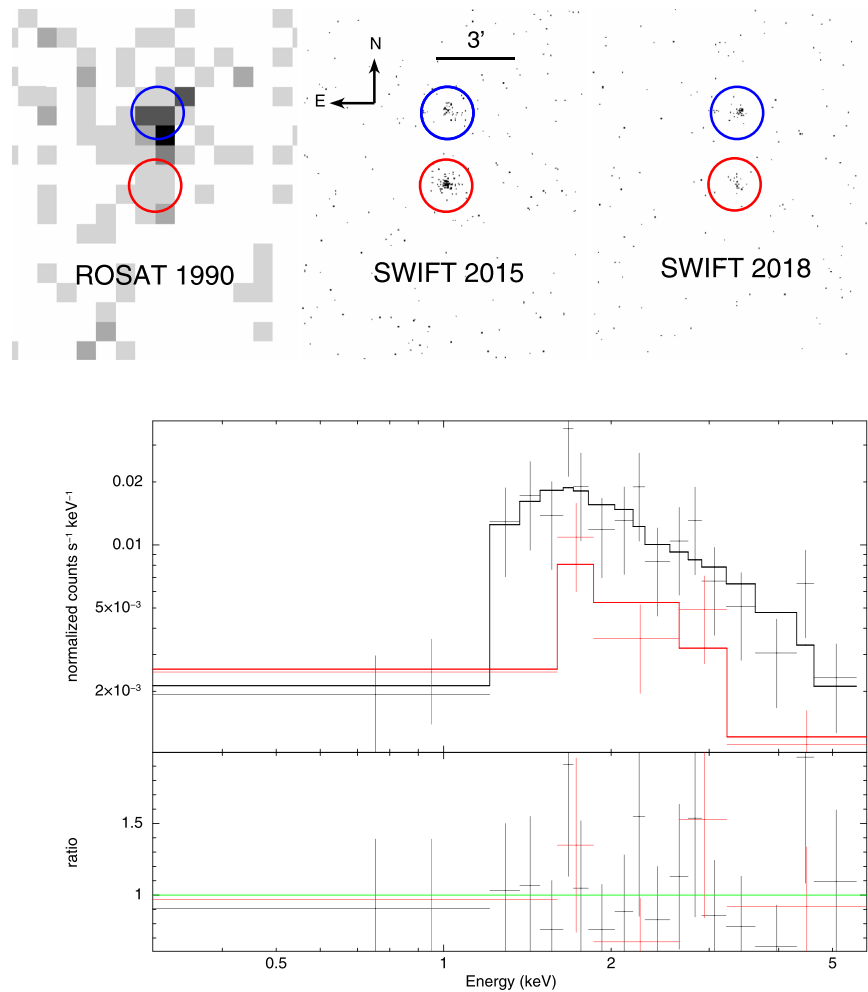
Figure 7. Top: X-ray images of MCG-02-04-026; one is from an observation taken in 1999 with ROSAT, and the other two are from observations taken in 2015 and 2018 with SWIFT. We label the positions of MCG-02-04-026 and the nearby Seyfert 1 galaxy using red and blue circles with radii of 1'. Bottom: X-ray spectra of MCG-02-04-026 from two observations in 2015 (black) and 2018 (red). For each spectrum, we plot the data (data point), the simple absorbed power-law model (lines), and the ratio between the data and the model.

Table 9
Parameters for Modeling the Swift Spectra

Parameter	2015	2018	2015 and 2018 (Tied)	
Γ	2.8 ± 0.6	3.3 ± 1.5	2.9 ± 0.6	
N_{H} $(10^{22}\,\mathrm{cm}^{-2})$	2.1 ± 0.7	2.5 ± 1.6	2.2 ± 0.6	
$L_{2-10\,\mathrm{keV}}$ $(10^{42}\,\mathrm{erg\,s}^{-1})$	$5.4^{+0.3}_{-2.4}$	<2.2	$5.2^{+0.3}_{-2.5}$	$2.5^{+0.2}_{-1.2}$
Cstat/dof	7.7/14	2.8/2	10.7/18	

they are typically not bright enough in the MIR band. For example, Szalai et al. (2019) collected MIR follow-up observations of hundreds of SNe and found that among them the brightest SN at 4.5 μm is SN 2010jl, with an absolute magnitude of -22.8, which is much dimmer than the MIR flare in MCG-02-04-026, with an absolute magnitude of -25.2 at 4.6 μm. We can also rule out the possibility of classical changing-look AGN events like those in Mrk 1018 and NGC 2627 because they evolve too slowly. The timescale of the variation in the MIR radiation of these changing-look AGNs typically exceeds $\sim$5 yr (Sheng et al. 2017), much longer than that of the MIR flare in MCG-02-04-026. We collected transient events meeting our constraints of energy budget and energy release timescale from the literature. These transient

events were listed in Section 1. Their interpretations include TDEs, SLSNe, and enhancement of the existing accretion flow onto the SMBH. Thus, we considered these three kinds of events as the possible nature of the primary event causing the MIR flare in MCG-02-04-026.

We must point out that it is highly challenging to further distinguish the three possibilities. The properties of the dust echo are not sensitive to the SED of the primary event because sufficiently thick dust absorbs almost all UV–optical photons equally. They are also not sensitive to the details of the UV–optical LC of the primary event, as the light-travel time effect blurs the MIR LC. Therefore, there are no other constraints on the nature of the primary event except for a rough energy budget and a rough energy release timescale based on only the MIR data. We detected a significant X-ray variation between the two observations in 2015 and 2018 with a factor of 2.4 ± 0.5, and the X-ray luminosities in 2–10 keV in both observations exceeded $10^{42}\,\mathrm{erg\,s}^{-1}$. Although such an X-ray variation is easy to explain as a result of an enhancement of the existing accretion flow onto the SMBH, we cannot accordingly rule out the possibilities of TDE or SLSNe. There are two reasons for this. One is that the X-ray variation is not necessarily related to the MIR flare considering that X-ray variations with a factor of only 2.4 are common among AGNs,
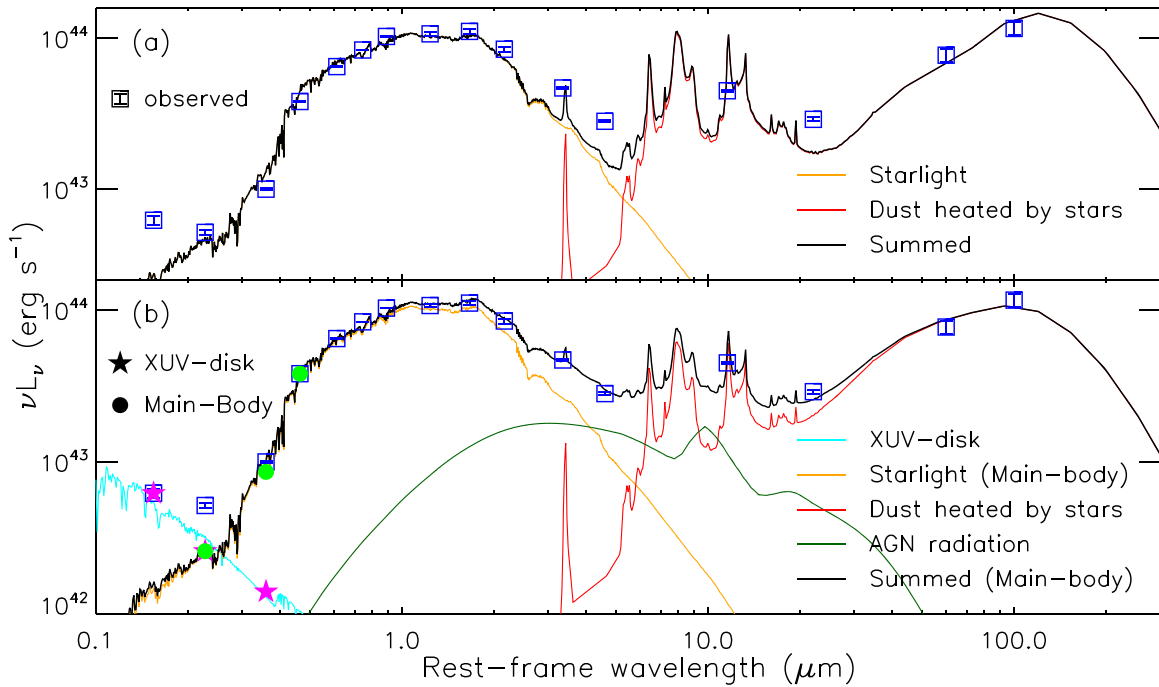
Figure 8. (a) Pre-flare SED of MCG-02-04-026 (blue boxes and data points) and a simple fit to it. We fit it using a simple stellar radiation model (black line), which consists of a starlight component (orange) and a dust radiation component (red). (b) Final fit to the pre-flare SED. We decomposed the radiation of MCG-02-04-026 in the FUV to g bands into two components, an XUV-disk component (magenta pentagram) and a main-body component (green circle). We show the simple stellar radiation model for the XUV disk (cyan line). We also show the final model for the main-body component (black line), which consists of a starlight component (orange), a stellar dust radiation component (red), and an AGN component (dark green).

while MIR flares like that in MCG-02-04-026 are rare. The other is that both TDEs and SLSNe can be accompanied with strong X-ray radiation (e.g., TDE Swift J164449.3+573451, Bloom et al. 2011; Burrows et al. 2011; SNe-IIn, Dwarkadas & Gruszko 2012). Therefore, the origin of the MIR flare cannot be clarified based on the available X-ray observations.

Although we cannot make a definitive conclusion about the nature of the transient event that caused the MIR flare in MCG-02-04-026, here we provided a way to explore the nature of similar events in the future. In our case, the first MIR excess was recorded (2014 July) 3–4 months after the predicted beginning time of the transient event. Hence, if future MIR surveys can have higher cadences than that of WISE, similar MIR flares will be caught in their earlier stages. Although the optical messages of the transient events will be blocked by the dust, the messages in the NIR band, where extinction is small (e.g., $A_K \sim 0.1 A_V$ for the Milky Way's extinction curve), can still be received. Therefore, after discovering MIR flares with MIR surveys, follow-up NIR observations should be taken as soon as possible to investigate the nature of the transient events.

6. Conclusions

We discovered an MIR flare using WISE data in the nearby edge-on disk galaxy MCG-02-04-026 at $z = 0.03485$. Before the MIR flare, MCG-02-04-026 is a dusty star-forming galaxy with an SFR of $\sim 3\ M_\odot\ \mathrm{yr}^{-1}$ and hosts a partially obscured ($E_{B-V} = 1.3$–1.8, $N_H \sim 2 \times 10^{22}\ \mathrm{cm}^{-2}$) active SMBH with $M_{BH} \sim 10^7\ M_\odot$. The MIR flare began in the first half of 2014, peaked around the end of 2015, and faded in 2017. Its position coincided with the galaxy nucleus with an accuracy of ~ 1 kpc. During the 3–4 yr, the MIR flare was roughly turning red. The MIR flare released a total energy in the range of 2.8–5.3 μm

($E_{2.8-5.3\ \mu\mathrm{m}}$) of 7.4×10^{50} erg. The total IR energy (E_{IR}) must be higher than this value, and a better estimation of the E_{IR} can be obtained to be $\sim 2 \times 10^{51}$ erg s^{-1} using blackbody models. Meanwhile, neither optical nor UV variation corresponding to the MIR flare was detected based on available data. X-ray net count rate changed by a factor of 2.4 ± 0.5 between two observations taken around the MIR flare, indicating a variation in the X-ray luminosity of the galaxy; however, we were not sure whether it is related to the MIR flare or not.

With a dust echo model in which radiative transfer is involved, we interpreted the MIR flare as the reradiation of dust heated by UV–optical radiation from a primary nuclear transient event. The model reproduces the MIR data and also explains the variation of the MIR color. The nondetection of optical or UV variation can be explained as the dust obscuration to the galaxy nucleus. We ruled out the possibility of radiation from a relativistic jet or dust heated by a shock. Therefore, we concluded that the nature of the MIR flare is the dust echo of the primary nuclear transient event.

The total energy of the primary transient event must be at least $\sim 10^{51}$ erg, and most of the energy must be released during less than ~ 3 yr. Such a transient event could be a TDE, an SLSN, or an enhancement of the existing accretion onto the SMBH. It is unlikely to be a normal SN or a classical changing-look AGN event with a timescale of tens of years.

MCG-02-04-026 provides a good example that an MIR blind survey can help find hidden nuclear transient events. Our analysis shows that, using only MIR data, it is possible to constrain some properties of the transient event, such as the energy budget and the energy release timescale. Future analysis of a large number of MIR flares like that seen in MCG-02-04-026 can improve our understanding toward hidden nuclear transient events, especially in active galaxies.

Table 10
Parameters for Modeling the Pre-flare SED with CIGALE

Parameter		Value
Stellar Radiation (XUV Disk)		
Age	Free	40 ± 30 Myr
τ	Free	60 ± 30 Myr
M_{star}	Inferred	$(1.7 \pm 1.1) \times 10^7 \, M_\odot$
SFR	Inferred	$0.5 \pm 0.1 \, M_\odot \, \mathrm{yr}^{-1}$
A_V(ISM)	Free	<0.03 mag
α	Fixed	2
Stellar Radiation (Main-body)		
t_0	Free	5500 ± 700 Myr
τ	Free	900 ± 130 Myr
M_{star}	Inferred	$(1.3 \pm 0.1) \times 10^{11} \, M_\odot$
SFR	Inferred	$2.8 \pm 0.3 \, M_\odot \, \mathrm{yr}^{-1}$
A_V(ISM)	Free	1.22 ± 0.06 mag
α	Free	2.1 ± 0.2
AGN Radiation		
r^a	Fixed	60
β^a	Fixed	-0.5
γ^a	Fixed	4.0
θ^a	Fixed	100
τ	Free	1.1 ± 0.6
ψ^b	Free	70 ± 10 deg
L_{AGN}	Inferred	$(3.5 \pm 0.6) \times 10^{43} \, \mathrm{erg \, s}^{-1}$

Notes.
[a] The fixed parameters in the model are the ratio of the maximum to minimum radii of the dust torus $r = 60$, parameters describing the dust density distribution $\beta = -0.5$ and $\gamma = 4$, and the opening angle of the dust torus $\theta = 100°$.
[b] The ψ value derived from the software is $20° \pm 10°$ because of an error in Fritz et al. (2006).

Appendix
The Approximate Empirical Formulae in the Dust Echo Model

The calculation of Lu16's model can be divided into four steps. Step 1 is to calculate the variation of grains radius a as functions of the distance R and retarded time t_r. Step 2 is to calculate the variation of the dust temperature T and emissivity $j_{IR}(\lambda)$ as functions of R and t_r. Step 3 is to calculate the variation of the attenuation of the IR radiation by other dust
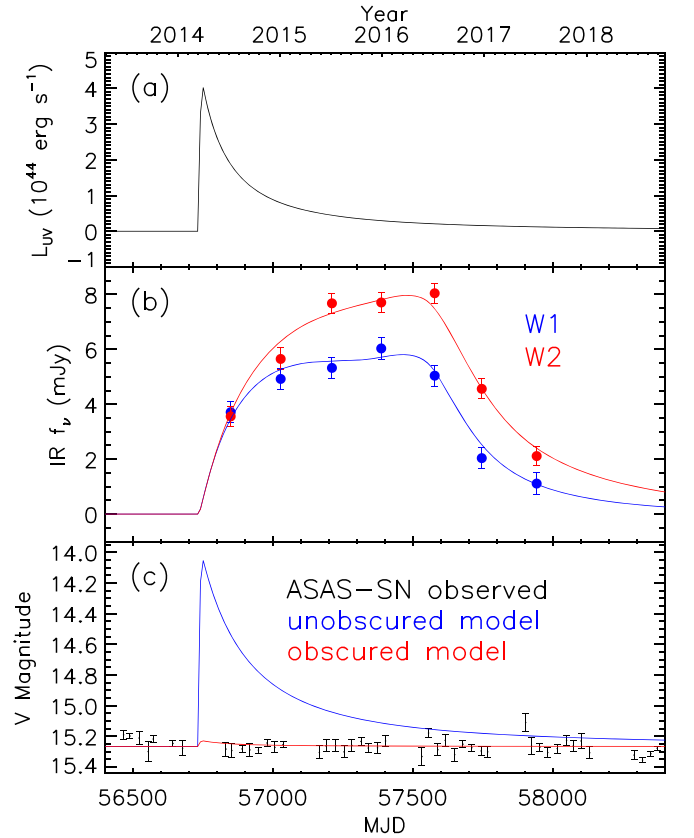
Figure 9. Dust echo model interpreting the observations. (a) Predicted UV–optical LC of the primary transient events. (b) Predicted MIR LCs and the observed data. (c) Predicted optical V-band LC and the LC from ASAS-SN observation. We show an unobscured model (blue) by assuming that the UV–optical radiation has a spectral shape of a blackbody curve with $T = 1.7 \times 10^4$ K and an obscured model (red) by assuming a dust extinction of $A_V = 4.7$ mag.

Table 11
Parameters for Modeling the MIR Data with the Dust Echo Model

Parameters	Form of $L(t)$		
	TDE	EXP	FLAT
a_0 (μm)	0.15	0.10	0.10
T_0 (MJD)	56740 ± 30	56710 ± 30	56660 ± 30
$\log L_{max}$ (10^{44} erg s^{-1})	5^{+3}_{-2}	6^{+2}_{-1}	2^{+2}_{-1}
$\log E_{tot}$ (10^{51} erg)	9^{+4}_{-2}	12^{+5}_{-3}	7^{+4}_{-2}
R_{sub} (100 lt-day)	3.7 ± 0.2	3.9 ± 0.2	4.3 ± 0.2
R_{out} (100 lt-day)	6^{+4}_{-2}	9^{+4}_{-2}	8^{+4}_{-2}
n_d (10^{-9} cm^{-3})	6^{+20}_{-3}	30^{+100}_{-10}	20^{+60}_{-10}
χ^2/dof	10.8/8	12.0/8	47.4/8

shells along the line of sight $\tau_{IR}(\lambda)$ as functions of position (R, θ) and t_r. Step 4 is to integrate the attenuated IR radiation to obtain observed LCs. Among these four steps, the first and third steps are the most time-consuming. In the first step, one needs to numerically solve the time-dependent differential equations. In the third step, one needs to track the IR photons and collect the properties of dust grains that the photons pass by (note that these properties vary with time) to calculate the attenuation. Thus, we used empirical formulae in the first and third steps.

First, we studied how the survival time of dust grains (t_{surv}) varies with distance R. We show the results from rigorous
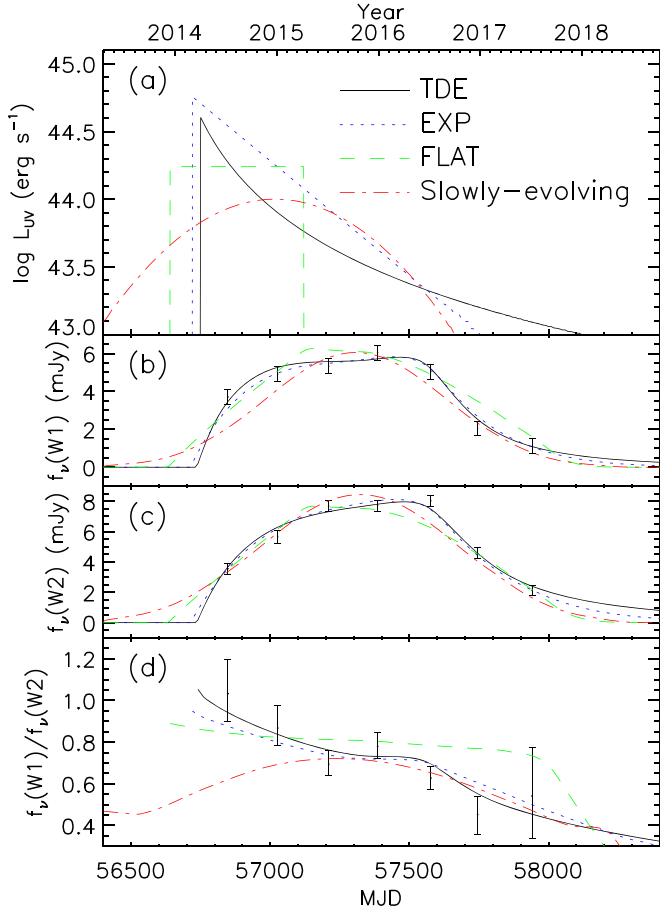
Figure 10. Comparison of models by assuming different UV–optical LCs. We show those of TDE form with black solid lines, those of EXP form with blue dotted lines, those of FLAT form with green dashed lines, and those of showly evolving form with red dashed–dotted lines. (a) UV–optical LCs. (b–d) Predicted LC in $W1$ band, in $W2$ band, and the ratio between them, and the observation.

simulations in Figure A1. We found that in a large space within the sublimation radius, t_{surv} grows nearly exponentially with the increase of R. We use the following functions as approximate empirical formulae (red lines in Figure A1):

$$t_{surv}(R) = \begin{cases} t_{flare} e^{\alpha(\frac{R}{R_{sub}}-1)}, & R_{in} < R < R_{sub} \\ \infty, & R > R_{sub}. \end{cases} \quad (A1)$$

The parameter t_{flare} stands for the duration of the high state of the transient event and is set to be

$$t_{flare} = \begin{cases} 0.15 E_{tot}/L_{max}, & \text{TDE form} \\ 0.3 E_{tot}/L_{max}, & \text{EXP form} \\ E_{tot}/L_{max}, & \text{FLAT form.} \end{cases} \quad (A2)$$

The parameter α depends on the form of UV–optical LCs: it is ~ 16.5 for the FLAT form and ~ 19 for the EXP and TDE forms. We fixed the α value according to the form of UV–optical LCs. We note that for $R < 0.8R_{sub}$, t_{surv} from the formula deviates from that from rigorous simulations. However, this deviation has little effect on the final results because the dust grains at positions $R < 0.8R_{sub}$ are destroyed soon and radiate little IR energy.

Then, we studied how the grain radius (a) varies with time. We show the results at four positions ($R/R_{sub} = 0.8, 0.9, 0.99,$
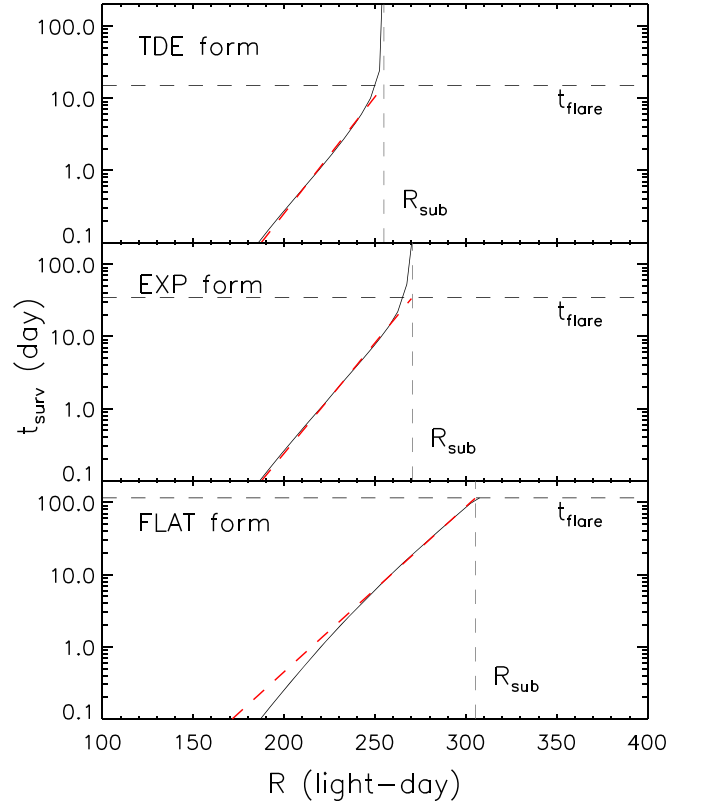

Figure A1. The survival time of dust grains (t_{surv}) varies with distance R. We show the results in three situations. The three situations assumed TDE, EXP, and FLAT forms of UV–optical LCs, respectively, and in all three situations, $L_{max} = 10^{45}$ erg s^{-1}, $E_{tot} = 10^{52}$ erg, $R_{in} = 100$ lt-day, $R_{out} = 600$ lt-day, $a_0 = 0.1$ μm, and $n_d = 10^{-8}$ cm^{-3}. We show the results from rigorous simulations with black solid lines and the approximate empirical formulae with red lines.
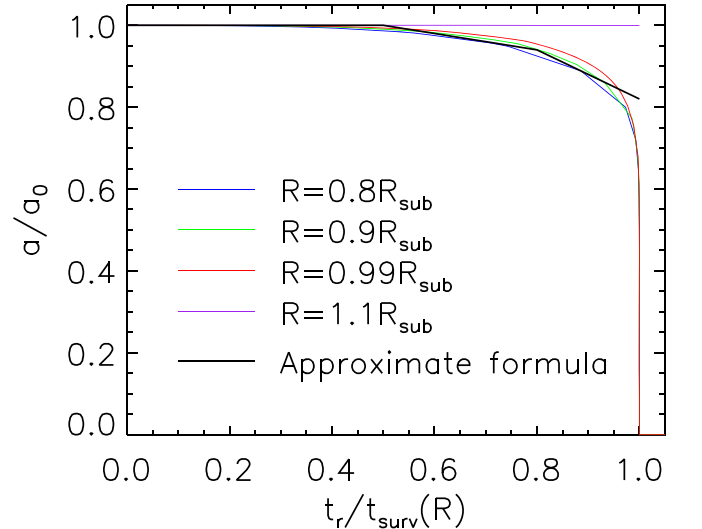

Figure A2. The grain radius (a) varies with retarded time (t_r). We show the results for dust grains in positions with distances R of 0.8, 0.9, 0.99, and 1.1 R_{sub} (blue, green, red, and purple lines, respectively) in the third situation described in the caption of Figure A1. We also show the piecewise function we defined as the approximate empirical formula.

and 1.1) from rigorous simulations in Figure A2. For the first three positions, the time is normalized by the local grain survival time ($t_{surv}(R)$), and for the last position, the time is normalized by the cutoff time of our simulation. We found that
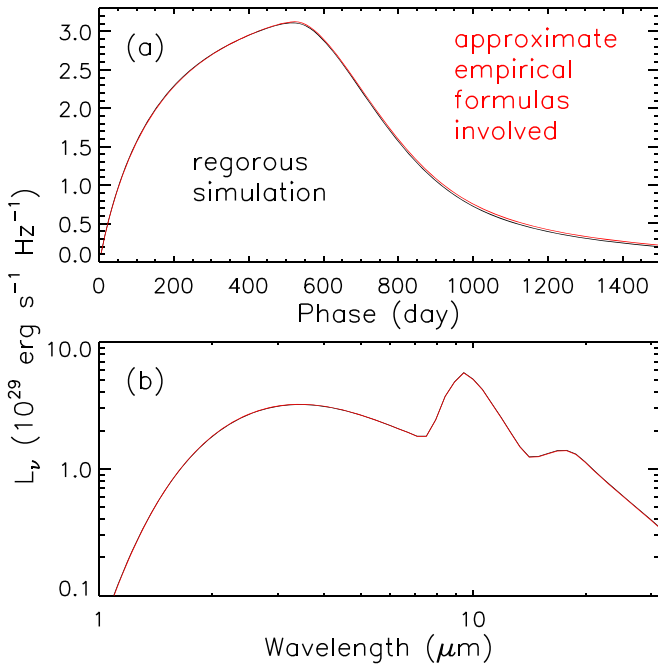
Figure A3. Comparison between the results of the rigorous simulations (black lines) and simulations with the approximate empirical formulae involved (red lines). We show the results of simulation in the first situation described in the caption of Figure A1. We show the LCs at 4 μm in the top panel and SEDs on the 510th day (close to the peak) in the bottom panel.

the variation in the grain radius (a) in positions inside the R_{sub} shows a consistent pattern: the grain radius first remains almost unchanged, then gradually decreases with increasing rate, and finally rapidly decreases to zero. We also found that the grain radius in positions outside the R_{sub} remains almost the same as the initial value. We described the variation of a with approximate empirical formulae. For grains in positions with $R < R_{sub}$, we used the following piecewise function (black line in Figure A2):

$$a(R, t_r) = \begin{cases} a_0, & x < 0.5 \\ a_0(1.1 - 0.2x), & 0.5 < x < 0.8 \\ a_0(1.42 - 0.6x), & 0.8 < x < 1 \\ 0, & x > 1 \end{cases}, \quad (A3)$$

where $x = \frac{t_r}{t_{surv}(R)}$. And for grains with $R > R_{sub}$, we set

$$a(R, t_r) = a_0. \quad (A4)$$

Finally, we studied how the IR optical depth $\tau_{IR}(\lambda)$ varied with position (R, θ) and retarded time (t_r). After testing, we found that one can make assumptions described by the following formula:

$$\tau_{IR}(R, \theta, t_r, \lambda) = \begin{cases} \tau_{IR}(R, \theta, \lambda, t_r = 0), & \theta \leqslant 90° \\ \tau_{IR}(R, \theta, \lambda, t_r = \infty), & \theta > 90°. \end{cases} \quad (A5)$$

The meaning of the formula is as follows: to always use the τ_{IR} value in the initial state for the hemisphere close to us, and to always use the τ_{IR} value in the final stable state for the hemisphere away from us. Our test shows that making these assumptions has little effect on the final results.

We verified the validity of our model by comparing the LCs and SEDs of IR radiation from the rigorous simulations and those from simulations in which the above approximate empirical formulae were used. We found that the differences

are within 2% in most cases, as shown by an example in Figure A3, and within 5% in extreme cases.

ORCID iDs

Luming Sun ⓘ https://orcid.org/0000-0002-7223-5840
Ning Jiang ⓘ https://orcid.org/0000-0002-7152-3621
Tinggui Wang ⓘ https://orcid.org/0000-0002-1517-6792
Hongyan Zhou ⓘ https://orcid.org/0000-0003-1956-9021
Liming Dou ⓘ https://orcid.org/0000-0002-4757-8622
Xiang Pan ⓘ https://orcid.org/0000-0002-6565-2339
Zhenfeng Sheng ⓘ https://orcid.org/0000-0001-6938-8670
Lin Yan ⓘ https://orcid.org/0000-0003-1710-9339

References

Alam, S., Albareti, F. D., Allende Priet, C., et al. 2015, ApJS, 219, 12
Almeyda, T., Robinson, A., Richmond, M., et al. 2017, ApJ, 843, 3
Assef, R. J., Prieto, J. L., Stern, D., Cutri, R. M., et al. 2018, ApJ, 866, 26
Becker, R. H., White, R. L., & Helfand, D. J. 1995, ApJ, 450, 559
Beichman, C. A., Neugebauer, G., Habing, H. J., Clegg, P. E., et al. 1988, Infrared Astronomical Satellite (IRAS) Catalogs and Atlases. Volume 1: Explanatory Supplement
Bell, E. F. 2003, ApJ, 586, 794
Bertin, E., & Arnouts, S. 1996, A&A, 117, 393
Blanchard, P. K., Nicholl, M., Berger, E., Guillochon, J., et al. 2017, ApJ, 843, 106
Bloom, J. S., Giannios, D., Metzger, B. D., Cenko, S. B., et al. 2011, Sci, 333, 203
Boquien, M., Burgarella, D., Roehlly, Y., Buat, V., et al. 2019, A&A, 622, 103
Bruzual, G., & Charlot, S. 2003, MNRAS, 344, 1000
Burrows, D. N., Kennea, J. A., Ghisellini, G., Mangano, V., et al. 2011, Natur, 476, 421
Caplar, N., Lilly, S. J., Trakhtenbrot, B., et al. 2017, ApJ, 834, 111
Charlot, S., & Fall, S. M. 2000, ApJ, 539, 718
Dale, D. A., Helou, G., Magdis, G. E., et al. 2014, ApJ, 784, 83
Denney, K. D., De Rosa, G., Croxall, K., et al. 2014, ApJ, 796, 134
Dou, L.-M., Wang, T.-G., Yan, L., et al. 2017, ApJ, 841, 8
Draine, B. T., & Lee, H. M. 1984, ApJ, 285, 89
Drake, A. J., Djorgovski, S. G., Graham, M. J., et al. 2019, MNRAS, 482, 98
Drake, A. J., Djorgovski, S. G., Mahabal, A., et al. 2009, ApJ, 696, 870
Drake, A. J., Djorgovski, S. G., Mahabal, A., et al. 2011, ApJ, 735, 106
Dwarkadas, V. V., & Gruszko, J. 2012, MNRAS, 419, 1515
Fitzpatrick, E. L. 1999, PASP, 111, 63
Fritz, J., Franceschini, A., & Hatziminaoglou, E. 2006, MNRAS, 366, 767
Gal-Yam, A. 2012, Sci, 337, 927
Gaskell, C.M. 2017, MNRAS, 467, 226
Gil de Paz, A., Madore, B. F., Boissier, S., et al. 2005, ApJ, 627, 29
Graham, M. J., Djorgovski, S. G., Drake, A. J., et al. 2017, MNRAS, 470, 4112
Greene, J. E., & Ho, L. C. 2005, ApJ, 630, 122
Gromadzki, M., Hamanowicz, A., Wyrzykowski, L., et al. 2019, A&A, 622, 2
Helfand, D.J., White, R.L., & Becker, R.H. 2015, ApJ, 801, 26
Ho, L. C. 1999, AdSpR, 23, 813
Hopkins, P. F., Richards, G. T., & Hernquist, L. 2007, ApJ, 654, 731
Jarrett, T. H., Chester, T., Cutri, R., et al. 2000, AJ, 119, 2498
Jiang, N., Wang, T.-G., Dou, L.-M., et al. 2020, ApJ, submitted
Jiang, N., Wang, T.-G., Mou, G.-B., et al. 2019, ApJ, 871, 15
Jiang, N., Wang, T.-G., Yan, L., et al. 2017, ApJ, 850, 63
Jiang, N., Zhou, H.-Y., Ho, L. C., et al. 2012, ApJ, 759, 31
Kalberla, P. M. W., Burton, W. B., Hartmann, D., et al. 2005, A&A, 440, 775
Kankare, E., Kotak, R., Mattila, S., et al. 2017, NatAs, 1, 865
Kewley, L. J., Groves, B., Kauffmann, G., & Heckman, T. 2006, MNRAS, 372, 961
Kochanek, C. S., Shappee, B. J., Stanek, K. Z., et al. 2017, PASP, 129, 4502
Komossa, S. 2015, JHEAp, 7, 148
Koss, M., Trakhtenbrot, B., Ricci, C., et al. 2017, ApJ, 850, 74
Kostrzewa-Rutkowska, Z., Jonker, P. G., Hodgkin, S. T., et al. 2018, MNRAS, 481, 307
Law, N. M., Kulkarni, S. R., Dekany, R. G., et al. 2009, PASP, 121, 1395
Lawrence, A. 2018, NatAs, 2, 102
Lawrence, A., Bruce, A. G., MacLeod, C., et al. 2016, MNRAS, 463, 296
Lu, H.-L., Zhou, H.-Y., Wang, J.-X., et al. 2006, AJ, 131, 790
Lu, W.-B., Kumar, P., & Evans, N. J. 2016, MNRAS, 458, 575
Mainzer, A., Bauer, J., Cutri, R. M., et al. 2014, ApJ, 792, 30

Mainzer, A., Grav, T., Bauer, J., et al. 2011, ApJ, 743, 156
Martin, D.C., Fanson, J., & Schiminovich, D. 2005, ApJ, 619, 1
Mattila, S., Pérez-Torres, M., Efstathiou, A., et al. 2018, Sci, 361, 482
McElroy, R. E., Husemann, B., Croom, S. M., Davis, T. A., et al. 2016, A&A, 593, 8
Meisner, A. M., Lang, D., & Schlegel, D. J. 2018, AJ, 156, 69
Merlin, E., Bourne, N., Castellano, M., et al. 2016, A&A, 595, 97
Merloni, A., & Heinz, S. 2007, MNRAS, 381, 589
Mineo, S., Gilfanov, M., Lehmer, B. D., et al. 2014, MNRAS, 437, 1698
Misselt, K. A., Clayton, G. C., & Gordon, K. D. 1999, ApJ, 515, 128
Moriya, T. J., Sorokina, E. I., & Chevalier, R. A. 2018, SSRv, 214, 59
Neugebauer, G., Habing, H.J., & van Duinen, R. 1984, ApJ, 278, 1
Panessa, F., Bassani, L., Cappi, M., et al. 2006, A&A, 455, 173
Pei, Y. C. 1992, ApJ, 395, 130
Peterson, B.M. 1997, An Introduction to Active Galactic Nuclei (Cambridge: Cambridge Univ. Press)
Rees, M. J. 1988, Natur, 333, 523
Salpeter, Edwin E. 1955, ApJ, 121, 161
Shappee, B. J., Prieto, J. L., Grupe, D., et al. 2014, ApJ, 788, 48
Sheng, Z.-F., Wang, T.-G., Jiang, N., et al. 2017, ApJL, 846, 7
Skrutskie, M.F., Cutri, R.M., & Stiening, R. 2006, AJ, 131, 1163
Stobbart, A.-M., Roberts, T. P., & Wilms, J. 2006, MNRAS, 368, 397
Storey, P. J., & Hummer, D. G. 1995, MNRAS, 272, 41
Szalai, T., Zsíros, S., Fox, O. D., et al. 2019, ApJS, 241, 38
Tadhunter, C., Spence, R., Rose, M., et al. 2017, NatAs, 1, 61
Trakhtenbrot, B., Arcavi, I., MacLeod, C. L., et al. 2019, ApJ, 883, 94
Wang, T.-G., Yan, L., Dou, L.-M., et al. 2018, MNRAS, 477, 2943
Wright, E. L., Eisenhardt, P. R. M., Mainzer, A. K., et al. 2010, AJ, 140, 1868
Yan, L., Wang, T.-G., Jiang, N., et al. 2019, ApJ, 874, 44
Yang, Qian, Shen, Yue, Liu, Xin, et al. 2019, ApJ, 885, 110
York, D. G., Adelman, J., Anderson, J. E., Jr., et al. 2000, AJ, 120, 1579